

# Canard Induced Mixed-Mode Oscillations in a Medial Entorhinal Cortex Layer II Stellate Cell Model

Horacio G. Rotstein\*

*Department of Mathematical Sciences,  
New Jersey Institute of Technology, Newark, NJ, 07102*

Martin Wechselberger<sup>†</sup>

*School of Mathematics and Statistics and Centre for Mathematical Biology,  
University of Sydney, NSW, 2006, Australia*

Nancy Kopell<sup>‡</sup>

*Department of Mathematics and Center for Biodynamics,  
Boston University, Boston, MA, 02215*

(Dated: May 13, 2008)

## Abstract

Stellate cells (SCs) of the medial entorhinal cortex (layer II) display mixed-mode oscillatory activity, subthreshold oscillations (small amplitude) interspersed with spikes (large amplitude), at theta frequencies (8 - 12 Hz). In this paper we study the mechanism of generation of such patterns in a SC biophysical (conductance-based) model. In particular, we show that the mechanism is based on the three-dimensional canard phenomenon and that the subthreshold oscillatory phenomenon is intrinsically nonlinear, involving the participation of both components (fast and slow) of a hyperpolarization-activated current in addition to the voltage and a persistent sodium current. We discuss some consequences of this mechanism for the SC intrinsic dynamics as well as for the interaction between SCs and external inhibitory inputs.

PACS numbers:

---

\*Electronic address: [horacio@oak.njit.edu](mailto:horacio@oak.njit.edu)

<sup>†</sup>Electronic address: [wm@maths.usyd.edu.au](mailto:wm@maths.usyd.edu.au)

<sup>‡</sup>Electronic address: [nk@math.bu.edu](mailto:nk@math.bu.edu)

## I. INTRODUCTION

The entorhinal cortex (EC) is the interface between the neocortex and the hippocampus [1], and it plays a very important role in orchestrating the flow of information between these two areas of the brain. Neocortical information flows to the hippocampus, to be processed, through the superficial layers (II and III) of the EC. The spiny stellate cells (SCs) are the most abundant principal cell type in layer II of the medial EC [1, 2]. These cells give rise to the main afferent fiber system to the hippocampus. In addition, in layer II of the EC grid cells are putative SCs. [3] (see references therein). Grid cell are principal neurons that exhibit multiple phase fields arranged in hexagonal patterns [4–6]. Their recent discovery implies that the EC contains a neural map of the spatial environment which is then transmitted to the hippocampus.

*In vitro* electrophysiological investigations have shown that, when depolarized, SCs develop small-amplitude rhythmic subthreshold membrane potential oscillations (STOs) at theta frequencies (8 - 12 Hz). If the membrane potential is depolarized further, then SCs fire action potentials at the peak of the STOs but not necessarily at every STO's cycle [7]. The amplitude of STOs and spikes differ roughly in an order of magnitude. We refer to the resulting temporal patterns (combination of STOs and spikes) as mixed-mode oscillations (MMOs). These are a distinctive property of SCs in layer II of the MEC [8–10] and they can be also found in *in vivo* electrophysiological studies [11].

Theta frequency STOs and MMOs in SCs are an intrinsic single cell phenomena [8] and have been shown to result from the interaction between two currents: A persistent sodium current ( $I_p$ ) and a hyperpolarization activated current ( $I_h$ ) [9]. Mathematical (conductance based) models, incorporating  $I_p$  and  $I_h$  in addition to the spiking currents (transient sodium, delayed rectifier potassium and leak) have been used to reproduce, via simulations, several aspects of the SC dynamics [12–14]. However, the mechanistic aspects of the generation of STOs and MMOs are still not fully understood.

The goal of this paper is to uncover the mechanism of generation of STOs and MMOs in the biophysical SC model proposed in [12], and to identify the key parameters controlling the transition among the various types of MMO patterns. We use analytical and computational techniques to show that, as hypothesized in [10], the generation of STOs and the onset of spikes in this model is governed by the three-dimensional canard phenomenon [15–17]. Qualitatively different mechanisms have been proposed to explain the generation of MMOs in other models. These are: break-up of an invariant torus [18], break-up (loss) of stability of a Shilnikov homoclinic orbit [19, 20], subcritical Hopf-homoclinic bifurcation [21, 22]. See also [17, 23] and other articles in the focus issue on MMOs introduced in [24] for a detailed discussion.

In Section II we provide some biophysical and mathematical background related to the generation of MMOs in SCs. We briefly describe the key experimental findings and the biophysical SC model we use in this paper. This model is a three-dimensional reduction [10] of the seven-dimensional model presented in [12]. The former, which we will refer to as the SC model, is a good approximation to the latter in the subthreshold regime where STOs and the onset of spikes are observed [10], thus allowing the investigation of the mechanisms of generation of STOs and MMOs. In addition, we explain some basic aspects on the canard phenomenon.

In Section III we describe the (dimensional) SC model and nondimensionalize it to uncover the multiple time-scale nature of the model. In particular, we show that the membrane potential evolves on a much faster time scale than the  $h$ -current gating variables ( $r_f$  and  $r_s$ ). Although the former is faster than the latter, there is no significant time scale separation between the two gates compared with the time scale separation introduced by the fast voltage dynamics. Therefore both gating dynamics of the  $h$ -current are considered as slow. For the remainder of this paper we use this dimensionless SC model. However, the results will be presented in terms of both the dimensional and dimensionless values of the relevant parameters. We also present the result of our simulations using this SC model showing MMO patterns and their corresponding phase-space diagrams.

In Section IV we analyze the mechanism of generation of MMOs in the SC model using numerical and analytical techniques. We show that for the relevant (biophysically plausible) parameters the SC model can be put in the analytic and geometric three-dimensional canard framework described in [16] for the generation of small amplitude oscillations (see also [17]). We describe this framework using notation tailored to the model. In addition, we describe the return mechanism necessary to bring trajectories back to the subthreshold regime after they escaped it towards the spiking one.

Our approach provides a geometric framework to qualitatively understand and predict the dynamic properties of the resulting MMO patterns. In particular, it allows us to study the dependence of these patterns on the relevant parameters: the  $I_h$  and  $I_p$  maximal conductances, the applied DC (constant) current, and the initial conditions of the participating variables in the subthreshold regime. These initial conditions reflect the reset properties of  $I_h$  after a spike has occurred. In addition, following the “canard approach” we explain how inhibitory pulses applied at different times after a spike has occurred may suppress some of the STOs of the unperturbed cell and advance the timing of the next spike. This type of calculation is the first step in the computation of spike-time response curves [12, 25, 26], which are used in the study of synchronization properties of small neural networks. We discuss our results and their implications for the understanding of SC dynamics in Section V.

## II. BACKGROUND

### A. Biophysics of subthreshold and mixed-mode oscillations in stellate cells

Voltage changes in single (isolated) neurons are the result of the flow of ionic currents into and out of the cells. Typically, three currents are involved in the generation of spikes: a transient sodium current ( $I_{Na}$ ), a delayed-rectifier potassium current ( $I_K$ ) and a leak current ( $I_L$ ) [27]. We refer to them as the standard spiking currents. Spikes are usually initiated by the activation of  $I_{Na}$  and terminated by its inactivation followed by the activation of  $I_K$ . Additional (non-standard or non-spiking) currents may be present and play various different roles in neural dynamics. Two non-standard currents have been implicated in the pacemaking of single-cell rhythmicity at theta frequencies: a persistent sodium current ( $I_p$ ) and an h-current ( $I_h$ ) [7–9, 13, 28–32] (see also references therein). The former constitutes a depolarization-activated fast inward current that precisely tracks voltage changes and provides the main drive for the depolarizing phase of the STOs. The latter is a hyperpolarization-activated (non-inactivating) current with slow activation kinetics, and it provides a delayed feedback effect that promotes resonance [33].

### B. Mixed-mode oscillations in a biophysically plausible stellate cell model

In recent work, Rotstein et al [10] showed that the biophysical (conductance based) SC model presented in [12] displays STOs and MMOs, and they initiated a mechanistic study of these phenomena using computational tools and dynamical systems ideas. In [10], reduction of dimension techniques were used to reveal a three-dimensional reduced model that is a good approximation to the “full”, seven-dimensional, SC model in the subthreshold regime where STOs and the onset of spikes occur. This reduced model describes the evolution of the membrane potential  $V$  (mV) and the two (fast and slow) h-current gating variables  $r_f$  and  $r_s$  (dimensionless). The latter describe the opening/closing of the h-current ion channels. In [10] it was found that both  $I_{Na}$  and  $I_K$  can be neglected in the subthreshold regime where STOs and MMOs are generated, and that the persistent sodium gating variable  $p$  has fast dynamics, so the adiabatic approximation can be made; i.e.,  $p$  can be well approximated by its corresponding voltage-dependent activation curve (see Section III). The resulting equations are presented in Section III, Eqs. (1)-(3). As mentioned above, they describe the generation of STOs and the onset of spikes, that occurs in the subthreshold regime, but they do not describe the spike dynamics and the early recovery from spiking, which belong to a different regime (where  $I_{Na}$  and  $I_K$  are the main active currents) [10]. If one is not interested in the spike details, the

dynamics of the SC can be approximately described by eqs. (1)-(3) supplemented with an “artificial spike”, operating in a much shorter time scale and reaching a peak of about 50 mV. This model has been called the Nonlinear Artificially Spiking (NAS) SC model [10], a class of models that includes the generalized integrate-and-fire models (see [10, 34, 35] for details). For simplicity, in the remainder of this paper we will refer to it as the SC model. When working with this (NAS) SC model one has to give appropriate threshold ( $V_{th}$ ) and reset ( $V_{rst}$ ) values. The former indicates that the trajectory arrived to the spiking regime. The latter is the voltage value after a spike has occurred, and represents the initial condition in the subthreshold regime. Note that, differently from other type of NAS models,  $V_{th}$  is not part of the mechanism of generation of action potentials which, as shown here and in [10], result from the dynamics of the so called “canard structure”.

### C. The canard phenomenon

Canards [36] were first studied in 2D relaxation oscillators [37–40], in particular in the van der Pol oscillator. There, the nature of the classical canard phenomenon is the transition from a small amplitude oscillatory state (STO) created in a Hopf bifurcation to a large amplitude relaxation oscillatory state within an exponentially small range of a control parameter. This transition, also called canard explosion, occurs through a sequence of canard cycles which can be asymptotically stable, but they are hard to observe in an experiment because of sensitivity to the control parameter. This is well known in the chemical literature where a canard explosion is classified as a hard transition [41, 42]. Therefore, 2D slow-fast systems display either STOs or large amplitude oscillations but no MMOs. However MMOs are possible by the addition of noise [43, 44].

Deterministic 3D slow-fast systems with two slow and one fast variables can produce MMOs [10, 16, 17, 23, 45–49] (See also the articles in the focus issue on MMOs introduced in [24]). One way to explain these patterns is based on a generalized canard phenomenon. The reason is that a special class of canards in 3D called canards of folded node (or folded saddle-node) type can be responsible for small amplitude oscillations [16, 46]. A good intuition for MMOs is that a system moves dynamically from a small amplitude oscillatory state to a relaxation oscillatory state and the feature of the large relaxation oscillation is to bring the system back to the basin of attraction of the small amplitude oscillatory state. A detailed explanation of this generalized canard phenomenon is given in Section IV.

### III. THE MODEL

#### A. Dimensional formulation

The dimensional equations are

$$C \frac{dV}{dt} = I_{app} - G_L (V - E_L) - G_p p_\infty(V) (V - E_{Na}) - G_h (c_f r_f + c_s r_s) (V - E_h), \quad (1)$$

$$\frac{dr_f}{dt} = \frac{r_{f,\infty}(V) - r_f}{\tau_{r_f}(V)}, \quad (2)$$

$$\frac{dr_s}{dt} = \frac{r_{s,\infty}(V) - r_s}{\tau_{r_s}(V)}, \quad (3)$$

where  $V$  is the membrane potential ( $mV$ ),  $C$  is the membrane capacitance ( $\mu F/cm^2$ ),  $I_{app}$  is the applied bias (DC) current ( $\mu A/cm^2$ ),  $I_L = G_L (V - E_L)$ ,  $I_p = G_p p_\infty(V) (V - E_{Na})$  and  $I_h = G_h (c_f r_f + c_s r_s) (V - E_h)$  [10]. The parameters  $G_X$  and  $E_X$  ( $X = L, p, Na, h$ ) are the maximal conductances ( $mS/cm^2$ ) and reversal potentials ( $mV$ ) respectively. The units of time are  $ms$ . The variables  $r_f$  and  $r_s$  are the h-current fast and slow gating variables and the parameters  $c_f$  and  $c_s$  represent the fraction of the total h-current corresponding to its fast and slow components respectively. Unless stated otherwise, we will use the following values for the parameters [10, 12]:  $E_{Na} = 55$ ,  $E_L = -65$ ,  $E_h = -20$ ,  $G_L = 0.5$ ,  $G_p = 0.5$ ,  $C = 1$ ,  $c_f = 0.65$  and  $c_s = 0.35$ . The functions  $r_{f,\infty}(V)$ ,  $r_{s,\infty}(V)$  and  $p_\infty(V)$  are the voltage-dependent activation/inactivation curves, and the functions  $\tau_{r_f}(V)$  and  $\tau_{r_s}(V)$  are the voltage-dependent time scales. They are given by  $r_{f,\infty}(V) = 1/(1 + e^{(V+79.2)/9.78})$ ,  $r_{s,\infty}(V) = 1/(1 + e^{(V+2.83)/15.9})^{58}$ ,  $p_\infty(V) = 1/(1 + e^{-(V+38)/6.5})$ ,  $\tau_{r_f}(V) = 0.51/(e^{(V-1.7)/10} + e^{-(V+340)/52}) + 1$  and  $\tau_{r_s}(V) = 5.6/(e^{(V-1.7)/14} + e^{-(V+260)/43}) + 1$ . The graphs of these functions are shown in Fig. 1.

#### B. Initial and threshold conditions in the subthreshold regime

The initial conditions in the subthreshold regime are given by the reset values of the participating variables after a spike has occurred. For  $r_f$  and  $r_s$  these reset values can be derived from the seven-dimensional stellate cell model [10]. More specifically, during a spike,  $V$  increases above zero to a value  $V \sim 50 mV$ . For these values of  $V$ ,  $r_{f,\infty}(V) \sim 0$  and  $r_{s,\infty}(V) \sim 0$ . (see Fig. 1-a). In addition, for these high values of  $V$ , both  $\tau_{r_f}(V)$  and  $\tau_{r_s}(V)$  are very small (see Fig. 1-b). Therefore, both  $r_f$  and  $r_s$  quickly decrease to values close to  $r_f \sim r_s \sim 0$ . The reset value of  $V \sim -80 mV$  is estimated from numerical simulations of the seven-dimensional

stellate cell model [10]. Unless stated otherwise, we take  $(V, r_f, r_s) = (-80, 0, 0)$  as the initial conditions of system (1)-(3) and we reset the trajectory to these values after each spike has occurred.

Since action potentials in this model are initiated at  $V \sim -50mV$  (see e.g., Figure 2) we may set the voltage threshold value  $V_{th}$  for this event to any value  $V > -50mV$ . Here we choose a value  $V_{th} = -40mV$  which is well above the initiation value. We emphasize that the spike results from the dynamics of the SC model and, consequently,  $V_{th}$  only indicates that a spike has occurred and is not a component of the mechanism of spike generation [10].

### C. Mixed-mode oscillations in the dimensional model

In Fig. 2 we illustrate various MMO patterns generated by the SC model. The voltage traces correspond to  $G_h = 1.5$ ,  $G_p = 0.5$  and a sequence of increasing values of  $I_{app}$ . We observe that the ratio of subthreshold oscillations to spikes decreases for increasing values of  $I_{app}$ . For values of  $I_{app}$  below and above these corresponding to Figs. 2-a and -e, the SC becomes silent and fully spiking respectively (no MMOs). We will use the notation  $1^s$  to indicate that an MMO pattern has a number  $s$  of STOs per spike.

Fig. 3 shows the three-dimensional phase space corresponding to the voltage traces presented in Fig. 2 (d) and (b). The  $V$ -nullsurface of the SC model is shown as well as the corresponding trajectories of MMO patterns. The trajectories move fast from their initial points towards the lower branch of the  $V$ -nullsurface and then along it towards the fold-curve (curve of knees of the  $V$ -nullsurface). Once the trajectories reach the vicinity of the fold-curve, they start to move almost parallel to the fold-curve and rotate generating STOs. Finally, the trajectories move rapidly in the direction of increasing values of  $V$ , eventually initiating a spike by activating  $I_{Na}$ . (The spiking dynamics belongs in a different regime and is not described by this reduced SC model.)

### D. Dimensionless formulation

Here we bring system (1)-(3) to a dimensionless form in order to uncover the different time scales in which the system operates. We first choose appropriate voltage and time scales,  $K_V$  and  $K_t$  respectively and define

$$v = \frac{V}{K_V}, \quad \bar{t} = \frac{t}{K_t}. \quad (4)$$

From a dimensional analysis point of view one would choose  $K_V$  as a combination of the model parameters. A more standard choice would be  $K_V = |E_K| = 90mV$ , which is the maximum,

in absolute value, reversal potential for the full SC model [10], and an upper bound for  $V$ . Here we choose  $K_V = 100 \text{ mV}$  which is a typical voltage scale for neuronal models, for easier comparison with the original full model as well as with the dimensional reduced model. The dimensionless voltage threshold and reset values are then given by  $v_{rst} = -80/K_V = -0.8$  and  $v_{th} = -40/K_V = -0.4$ . The relevant voltage range for our model in terms of the dimensionless variable  $v$  is therefore  $[-0.8 : -0.4]$ . We define

$$T_f = \min_{v \in [-0.8: -0.4]} \tau_{r_f}(K_V v), \quad T_s = \min_{v \in [-0.8: -0.4]} \tau_{r_s}(K_V v), \quad (5)$$

and we choose  $K_T = T_f \sim 30 \text{ ms}$  as a typical (slow) time scale (see Fig. 1-b).

We also define a reference maximal conductance  $K_G = 1.5 \text{ mS/cm}^2$ , which is at the top of the physiologically plausible scale for maximal conductances. This is the value of  $G_h$  we used in the simulations presented in Figs. 2 and 3. We define the following dimensionless variables, parameters and functions

$$\bar{E}_L = \frac{E_L}{K_V}, \quad \bar{E}_{Na} = \frac{E_{Na}}{K_V}, \quad \bar{E}_h = \frac{E_h}{K_V}, \quad (6)$$

$$\bar{G}_p = \frac{G_p}{K_G}, \quad \bar{G}_h = \frac{G_h}{K_G}, \quad \bar{G}_L = \frac{G_L}{K_G}, \quad \bar{I}_{app} = \frac{I_{app}}{K_G K_V}, \quad (7)$$

$$\epsilon = \frac{C}{K_T K_G} = \frac{C}{T_f K_G} \sim 0.023 \ll 1, \quad \eta = \frac{K_T}{T_s} = \frac{T_f}{T_s} \sim 0.286, \quad (8)$$

$$\bar{r}_{f,\infty}(v) = r_{f,\infty}(K_V v), \quad \bar{r}_{s,\infty}(v) = r_{s,\infty}(K_V v), \quad \bar{p}_\infty(v) = p_\infty(K_V v), \quad (9)$$

$$\bar{\tau}_{r_f}(v) = \frac{\tau_{r_f}(K_V v)}{T_f}, \quad \bar{\tau}_{r_s}(v) = \frac{\tau_{r_s}(K_V v)}{T_s}. \quad (10)$$

Substituting eqs. (4-10) into eqs. (1-3) and deleting the “bar” sign one gets

$$\epsilon \frac{dv}{dt} = I_{app} - G_L (v - E_L) - G_p p_\infty(v) (v - E_{Na}) - G_h (c_f r_f + c_s r_s) (v - E_h), \quad (11)$$

$$\frac{dr_f}{dt} = \frac{r_{f,\infty}(v) - r_f}{\tau_{r_f}(v)}, \quad (12)$$

$$\frac{dr_s}{dt} = \eta \frac{r_{s,\infty}(v) - r_s}{\tau_{r_s}(v)}. \quad (13)$$

System (11)-(13) is a fast-slow system with  $v$  evolving on the fast time scale and both  $r_f$  and  $r_s$  evolving on a slow scale. These two variables evolve on a similar slow time-scale, as it becomes apparent by comparing the values of  $\epsilon$  and  $\eta$  ( $\epsilon \ll \eta$ ).

#### IV. THE MECHANISM OF GENERATION OF MIXED-MODE OSCILLATIONS

Mixed-mode oscillations (MMOs) consist of subthreshold oscillations (STOs) interspersed with spikes (large amplitude oscillations occurring on a faster time scale). In this section we show that the generation of MMOs in the SC model (11)-(13) is governed by the canard phenomenon. In our explanation we will follow [16, 17]. We use notation tailored to the model. For simplicity we call

$$f(v, r_f, r_s) = I_{app} - G_L (v - E_L) - G_p p_\infty(v) (v - E_{Na}) - G_h (c_f r_f + c_s r_s) (v - E_h), \quad (14)$$

$$g(v, r_f) = \frac{r_{f,\infty}(v) - r_f}{\tau_{r_f}(v)}, \quad (15)$$

$$h(v, r_s) = \eta \frac{r_{s,\infty}(v) - r_s}{\tau_{r_s}(v)}. \quad (16)$$

As we show below, the existence of MMOs for the SC model (11)-(13) is guaranteed by Theorem 4.1 or Theorem 4.2 in [17]. These theorems require that the  $v$ -nullsurface (which we will refer to as  $S$ ) is folded (parabolic cylinder shape). STOs occur in the vicinity of the fold-curve  $L$  (the curve of knees of  $S$ ), defined as the set of points  $\{p \in S : f_v(p) = 0, f_{vv}(p) < 0\}$ . The lower ( $S_a$ ) and upper ( $S_r$ ) branches of the folded manifold  $S$  are attracting ( $f_v < 0$ ) and repelling ( $f_v > 0$ ) respectively. After a finite number of STOs the trajectory moves away from  $S$  and escapes the subthreshold regime towards the spiking one as we explain in Section IV B. For MMOs to occur, the trajectory should be able to come back to the subthreshold regime; i.e., a suitable return mechanism should bring the trajectory back to a region of  $S$  where it can evolve towards its curve of knees  $L$  (setting the initial conditions in the subthreshold regime). Different models may have different return mechanisms. The one corresponding to this model was described in Section III B. In the following sections we describe the mechanism of generation of STOs and the onset of spikes for system (11)-(13) and we show their dependence on some of the parameters of the model.

We are mainly interested in understanding the contribution of  $I_h$  to the observed mixed-mode oscillatory patterns since  $I_h$  is known to change with development and neuromodulators [50]. Changes in the amounts of  $I_h$  are reflected in changes in the maximal conductances  $G_h$ . Other effects include changes to the activation curves ( $r_{f,\infty}(V)$  and  $r_{s,\infty}(V)$ ) and the voltage-dependent time scales through the values of  $\epsilon$  and  $\eta$  or the reset properties of  $I_h$  (initial conditions in the subthreshold regime). Changes in these values may affect the relative number of subthreshold oscillations per spike, the oscillatory frequency and the amplitude of the STOs.

## A. A geometric singular perturbation theory approach

The SC model (11)-(13) is a singularly perturbed system with one fast ( $v$ ) and two slow ( $r_f, r_s$ ) variables. This system evolves on a slow time scale  $t = \varepsilon\tau$ . The limiting problem  $\varepsilon \rightarrow 0$  on this slow time scale  $t$  is called the *reduced problem* and describes the evolution of the slow variables ( $r_f, r_s$ ). The phase space of the reduced problem is the critical manifold  $S$  defined by  $S := \{(v, r_f, r_s) \in \mathbb{R}^3 : f(v, r_f, r_s) = 0\}$ ; i.e.,  $S$  is the  $v$ -nullsurface. We represent it by

$$r_f = \phi(v, r_s) = \frac{I_{app} - G_L (v - E_L) - G_p p_\infty(v) (v - E_{Na})}{c_f G_h (v - E_h)} - \frac{c_s}{c_f} r_s. \quad (17)$$

Fig. 4 illustrates  $S$  for two values of  $I_{app}$  and other physiologically plausible parameters.

The second limiting problem is called the *layer problem*, and it is obtained by rescaling time ( $\tau = t/\varepsilon$ ) in system (11)-(13) and setting  $\varepsilon \rightarrow 0$ . The layer problem describes the evolution of  $v$  on the fast time scale for fixed values of the gating variables ( $r_f, r_s$ ), i.e. the slow variables are considered as parameters in this singular limit. Note that the manifold  $S$  is a manifold of equilibria for the layer problem.

These two limiting problems, the reduced problem (2D) and layer problem (1D), are lower dimensional than the full problem (3D) and are therefore more amenable to analysis. Geometric singular perturbation theory [17, 51, 52] provides a way to piecing together the information obtained from these lower dimensional problems in order to provide a unified global description of the observed mixed-mode oscillations in the full 3D system.

## B. Layer problem

By rescaling time ( $\tau = t/\varepsilon$ ) in eqs. (11)-(13) and setting  $\varepsilon = 0$  one obtains the layer problem which describes the fast dynamics away from the critical manifold  $S$ , represented by eq. (17) :

$$\frac{dv}{d\tau} = f(v, r_f, r_s), \quad (18)$$

$$\frac{dr_f}{d\tau} = 0, \quad (19)$$

$$\frac{dr_s}{d\tau} = 0. \quad (20)$$

Trajectories of the layer problem starting at an initial point  $(v_0, r_{s,0}, r_{f,0})$  evolve along one dimensional sets  $(v, r_{s,0}, r_{f,0})$ , called fast fibers, near the critical manifold.

$S$  is a manifold of equilibria for the layer problem; i.e., the intersection points between  $S$  and vertical lines containing the fast fibers define the fixed-point corresponding to each trajectory. By linearizing the layer problem at  $S$  one obtains information about the transient behaviour of the solutions along the fast fibers. As we illustrate in Fig. 4, the critical manifold  $S$  is folded. This remains true for parameter variations in the physiologically plausible regime (data not shown). The lower ( $S_a$ ) and upper ( $S_r$ ) branches of the folded manifold  $S$  are attracting ( $f_v < 0$ ) and repelling ( $f_v > 0$ ) respectively. Fig. 4 also illustrates that changes in the key parameters of the model (e.g.  $I_{app}$ ) do not affect the shape of the folded slow manifold  $S$  significantly.

### C. Initial conditions of the reduced problem on the critical manifold

The relevant trajectory in the subthreshold regime starts at  $(v, r_f, r_s) = (-0.8, 0, 0)$  (see Sections I and III D). This trajectory is projected on  $S_a$  along the corresponding fast fiber to the equilibrium point  $(v_0, r_{f,0} = 0, r_{s,0} = 0)$  of the layer problem. This point on the critical manifold is then used as the initial condition of the reduced flow corresponding to the initial condition  $(v, r_f, r_s) = (-0.8, 0, 0)$ . Note that we use the same notation for initial conditions on the critical manifold  $S$  as for the initial conditions for problem (11)-(13). Figure 4-b shows the critical manifold intersected with the plane  $r_s = 0$ . For  $r_f = r_s = 0$  as initial conditions (reset values) then this figure shows that  $V \sim -70mV$  ( $v \sim -0.7$ ) corresponds to the intersection of the fast fiber through  $r_f = r_s = 0$  with the critical manifold. Therefore we will take  $v_0 \sim -0.7$  as initial condition for the reduced problem. The exact initial condition on the critical manifold depends on the parameters of the model. We make the appropriate calculations for each parameter set.

### D. The reduced flow

The reduced flow is obtained by setting  $\epsilon = 0$  in eq. (11). System (11)-(13) becomes

$$0 = f(v, r_f, r_s), \quad (21)$$

$$\frac{dr_f}{dt} = g(v, r_f), \quad (22)$$

$$\frac{dr_s}{dt} = h(v, r_s). \quad (23)$$

These equations describe the evolution of  $r_f$  and  $r_s$  on the critical manifold  $S$  defined by eq. (17).

Trajectories evolve on the slow manifold  $S$  (actually on  $S_a$ ), from their initial conditions  $(v_0, r_{f,0}, r_{s,0})$ , towards the fold-curve  $L$ . Since  $S$  is given as a graph  $\phi(v, r_s)$  we project the reduced system (21)-(23) onto the  $(v, r_s)$ -plane. By implicitly differentiating the function  $f(v, r_f, r_s) = 0$  we obtain the reduced system

$$\begin{pmatrix} -f_v v' \\ r'_s \end{pmatrix} = \begin{pmatrix} f_{r_f} g + f_{r_s} h \\ h \end{pmatrix}_{r_f=\phi(v,r_s)}. \quad (24)$$

This system is singular along the fold-curve  $L$  ( $f_v = 0$ ). Therefore we rescale time by a factor  $-f_v$  to obtain the desingularized system

$$\begin{pmatrix} \dot{v} \\ \dot{r}_s \end{pmatrix} = \begin{pmatrix} f_{r_f} g + f_{r_s} h \\ -f_v h \end{pmatrix}_{r_f=\phi(v,r_s)}, \quad (25)$$

where the overdot represents differentiation with respect to this new time. Note that system (25) has the same phase portrait as system (24) but the orientation of the flow on  $S_r$  (unstable slow manifold) has to be reversed due to the rescaling of time.

There are two types of singularities in system (25): regular and folded singularities. Regular singularities are given by  $h = 0$  and  $g = 0$  and are therefore also equilibria of the reduced flow (24). These singularities will (generically) persist under small perturbations in system (11)-(13) with  $\epsilon \ll 1$ . On the other hand, folded singularities are given by  $f_v = 0$ , which defines the fold-curve  $L$ , and  $f_{r_f} g + f_{r_s} h = 0$  (for points  $\bar{p}$  on  $L$ ). Each folded singularity is classified as a folded saddle, folded node or folded saddle-node based on its classification as a saddle, node or saddle-node as an equilibrium of (25). Folded singularities are not equilibria of the reduced system (24). However, as shown in [15, 17], their presence gives the opportunity for the reduced flow to cross from  $S_a$  to  $S_r$  through  $L$  in finite time. If there are no folded singularities, then trajectories of the reduced flow which arrive at the fold-curve subsequently jump along the fast fibers and escape the subthreshold regime without generating any STO.

As we show in Section IV F, the singularities found in the SC model, for the relevant biophysically plausible parameters, are folded nodes (or folded saddle-nodes). For more details about folded singularities we refer to [15–17, 45]. Associated with a folded node there exists a whole sector of trajectories, called singular canards, that are able to pass from  $S_a$  to  $S_r$  through the folded node. This sector is called the singular funnel. Two singular canards are related to the eigendirections of the folded node. They are the weak and strong canards. They correspond to the smallest and largest (in absolute value) eigenvalues respectively. The singular funnel is bounded by the fold-curve  $L$  and the strong canard. The latter is the strong

stable invariant manifold of the folded node. The canards and funnel existing from  $\epsilon > 0$  (sufficiently small) arise as perturbation of their singular counterparts. Only trajectories entering the funnel are able to rotate around the weak canard (see Fig. 5). For a geometric description of this phenomenon we refer the reader to [16, 17].

### E. Existence of MMOs

Based on the singular limit behavior of solutions in both the reduced and the layer problem, Brøns et al. [17] provided a theorem that guarantees the existence of MMOs for system (11)-(13) with a sufficiently small  $0 < \epsilon \ll 1$ . This theorem is based on the following assumptions:

**Assumption 1:** The singularly perturbed system is (locally) a folded surface, as in system (11)-(13) for parameters sets in the physiologically plausible range. This was shown in Section IV B.

**Assumption 2:** The problem possesses a folded node singularity. In Section IV F we will determine parameter ranges (in the physiologically plausible regime) for which folded nodes exist.

**Assumption 3:** There exists a singular periodic orbit (see Figure 5) which consists of a segment on  $S_a$  (blue) within the singular funnel (shadowed region) with the folded node singularity (black circle) as an endpoint, fast fibers (red) of the layer problem and a global return mechanism (green). The global return mechanism for the SC model was described in Sections III B and IV C

If Assumptions 1–3 are fulfilled then Theorem 4.1 in [17] predicts maximal  $1^s$  MMO patterns (for sufficiently small  $\epsilon$ ). There are two limiting cases of the theory related to Assumptions 2 and 3. In Assumption 3, if the global return mechanism is on the border of the singular funnel (the brown trajectory in Fig. 5) then Theorem 4.2 in [17] predicts sub-maximal MMO patterns. In the folded saddle-node limit, Assumption 2 is violated but we still expect the existence of MMOs (with a large number of STOs). The theory for this limiting case has still to be developed but we can use the folded node theory to make qualitative predictions of MMOs. We will discuss both limiting cases in Section IV H.

### F. The folded node singularity and the canard phenomenon

In order to look for parameter ranges in which system (11)-(13) possesses a folded node singularity, we numerically calculated the desingularized reduced flow corresponding to (25)

for various values of  $G_h$  and  $I_{app}$ . We used XPPAUT [53] for these computations and a Runge-Kutta method of order II [54] for the numerical simulations of the 3D system (11)-(13). The results are given in terms of the dimensional values of the parameters. Their corresponding dimensionless values are given in parenthesis. We will first consider the case  $G_h = 1.5$  (1.0) for which we found the existence of

- a regular node singularity on  $S_a$ , a folded saddle singularity and a regular node singularity on  $S_r$  for  $I_{app} < -2.64$  ( $-0.0176$ ).
- a folded saddle-node singularity and a regular node singularity on  $S_r$  for  $I_{app} \approx -2.64$ .
- a regular saddle singularity on  $S_r$ , a regular node singularity on  $S_r$  and a folded node singularity for  $-2.64 < I_{app} < -1.92$  ( $-0.0128$ ).
- a saddle-node singularity on  $S_r$  and a folded node singularity for  $I_{app} \approx -1.92$  ( $-0.0128$ )
- a folded node singularity for  $-1.92 < I_{app} < -1.86$  ( $-0.0124$ ).
- a folded focus singularity for  $I_{app} > -1.86$ .

Therefore a folded node singularity exists for values of  $I_{app} \in (-2.64, -1.86)$ . To each folded node corresponds a singular funnel which is bounded by the strong canard and the fold-curve. The strong canard is an invariant manifold of the folded node, it is a separatrix of the flow on the reduced phase space  $S$ , and therefore a borderline for qualitatively different behaviors. Note that the strong canard is related to the strong eigendirection of the folded node and is therefore unique.

Fig. 6 shows the folded node, the singular strong canard, the fold-curve and the singular funnel for three values of  $I_{app}$  and the same values of both  $G_h$  and the initial conditions on  $S_a$ . In Fig. 6-a, an initial condition within the singular funnel will be ‘funneled’ into the folded singularity and gives the possibility of STOs [16] for  $\epsilon > 0$ . The corresponding voltage trace showing STOs is given in Fig. 7-a. If an initial condition is outside the funnel (Figure 6-c), then the reduced flow will reach the fold-curve at an (ordinary) *jump point* where solutions jump off the fold and follow a fast fiber, which leads to the spiking regime without displaying STOs. The corresponding voltage trace showing only spiking activity is given in Fig. 7-c. Figs. 6-b and 7-b correspond to a trajectory within the funnel but very close to its boundary. The voltage trace shows only one STO per spike. From Fig. 6 and the voltage traces showed in Fig. 7 we observe that as we increase  $I_{app}$  the folded node moves to the left and, accordingly, the strong canards (separatrices) intersect the  $v$ -axis at higher values. As this occur, trajectories starting at approximately the same initial values on the critical manifold,  $v \in (-0.69, -0.68)$ ,

evolve closer to the strong canard, decreasing their number of STOs (per spike) and, for higher values of  $I_{app}$ , they are left outside the funnel and generate only spiking activity.

Fig. 8 shows the folded nodes and corresponding strong canards for various values of  $I_{app}$ . The range of values of  $v_0$  whose corresponding trajectories will be attracted to the funnel shrinks as  $I_{app}$  increases. For example, the singular limit analysis predicts that trajectories on the slow manifold with initial conditions  $(r_f(0), r_s(0)) = (0, 0)$  and the corresponding values of  $v_0$  will not display STOs for  $I_{app} > -2.25$  and for  $I_{app} < -2.64$  (corresponding to a lower bound where a folded node singularity exists). Our simulations of the SC model (11)-(13) show the existence of MMOs for  $-2.57 < I_{app} < -2.27$ ; i.e., both the onset of MMOs and the change from MMOs to relaxation oscillations occur for slightly higher values than theoretically predicted. However, in both cases these values are within the order of the singular perturbation parameter  $\epsilon$ , and therefore justify the singular prediction made above.

The observed MMO parameter window  $-2.57 < I_{app} < -2.27$  for the SC model is also in good agreement with the MMO parameter window  $-2.7 < I_{app} < -2.4$  of the full seven-dimensional model. The (small) shift to more depolarized values in the SC model (11)-(13) is basically explained by the lack of the depolarized current  $I_{Na}$  given by the full seven-dimensional model. A more detailed comparison of the two models can be found in [55].

### G. Transition between subthreshold oscillatory regimes as a consequence of changes in the h-current reset properties

Changes in the h-current reset properties are reflected in changes in the initial values of its gating variables  $r_f$  and  $r_s$  in the subthreshold regime, and in particular on the slow manifold. Here we show how this affects the subthreshold oscillatory properties of the MMO  $1^s$  patterns, in particular the number of subthreshold oscillations per spike. This number  $s$  depends on the ratio  $\mu = \lambda_1 / \lambda_2 < 1$  between the eigenvalues corresponding to the weak and strong eigendirections of the folded node in system (25). In the case  $\mu < 1/3$ , it was shown in [16] that singularly perturbed systems like (11)-(13) possess  $\lfloor (1 - \mu)/(2\mu) \rfloor$  *secondary canards* besides the two primary (weak and strong) canards, where  $\lfloor (1 - \mu)/(2\mu) \rfloor$  denotes the greatest integer less or equal than  $(1 - \mu)/(2\mu)$ .

These secondary canards divide the singular funnel into sub-sectors (see Fig. 9). Each of them is associated with a specific value of  $s$  in the MMO  $1^s$  patterns; i.e., trajectories entering different sectors display a different number of STOs per spike. This number increases from the sector bounded by the strong canard to the sector bounded by the fold-curve. The maximum number of STOs is defined by  $s^* := (1 + \mu)/(2\mu)$  which is a singular limit prediction. Table I shows the number of secondary canards and maximum number  $s^*$  STOs for  $G_h = 1.5$  (1.0)

$I_{app}$	$\mu$	$(1 - \mu)/(2\mu)$	$s^*$
-2.6	0.0097	51	52
-2.5	0.0480	9	10
-2.4	0.0917	4	5
-2.3	0.1430	2	3
-2.25	0.1725	2	3
-2.1	0.2842	1	2
-2.0	0.3940	0	1

TABLE I: Singular limit predictions of number of secondary canards and maximum number  $s^*$  of STOs for  $G_h = 1.5$  (1.0) under the variation of  $I_{app}$

under the variation of  $I_{app}$ .

As a consequence of an increase in the initial values of  $r_f$  and  $r_s$ , the initial voltage on  $S$  also changes, and trajectories may enter a sector corresponding to a higher or lower number of STOs. We illustrate this in Figs. 9 to 11. We first vary  $r_s(0)$  and keep  $r_f(0) = 0$  unchanged for  $I_{app} = -2.4$  (dimensionless value:  $I_{app} = -0.0160$ ). We illustrate this schematically in Fig. 9-a. The voltage traces are presented in Fig. 10. The initial conditions on the slow manifold  $S$  approximate a line passing through the points  $(v_0, r_{f,0}, r_{s,0}) = (-0.69, 0, 0)$  and  $(v_0, r_{f,0}, r_{s,0}) = (-0.67, 0, 0.03)$  (dashed segment in Fig. 9-a). We observe that the transition from MMO to only spiking patterns occurs for a value of  $r_s(0)$  slightly higher than 0.02, and the number  $s$  of STOs per spike decreases as we increase  $r_s(0)$ . The result of our simulations (Fig. 10) are in agreement with this prediction. In Figs. 9-b and 11 we vary  $r_f(0)$  and keep  $r_s(0) = 0$  unchanged for  $I_{app} = -2.25$  (dimensionless value:  $I_{app} = -0.0150$ ). The initial conditions on  $S$  are located on the  $v$ -axis at the points  $(-0.69, 0, 0)$ ,  $(-0.66, 0.025, 0)$  and  $(-0.63, 0.05, 0)$  (dashed vertical segment in Fig. 9-b). This dashed vertical segment crosses the strong canard at  $v \sim -0.675$ . According to this, the transition from  $1^1$  to  $1^0$  (spikes only) MMO patterns occurs for  $r_s$  lower than 0.025. The results of our simulations (Fig. 11) are in agreement with this prediction.

## H. MMO theory and the dependence on the singular perturbation parameter

The existence results on MMOs presented here are based on singular perturbation theory and hold for sufficiently small singular perturbation parameter  $0 < \epsilon \ll 1$  [16, 17]. In particular, Theorem 4.1 in [17] states that if Assumptions 1-3 are fulfilled then maximal  $1^{s^*}$  MMOs

are expected for sufficiently small  $\epsilon$ . Sufficiently small  $\epsilon$  means here that  $\mu \gg \sqrt{\epsilon}$  for the eigenvalue ratio of the folded node as well as that  $\delta \gg \sqrt{\epsilon}$  where  $\delta$  defines the distance of the initial condition on  $S^a$  from the strong canard (relative position of the global return within the funnel). The  $\sqrt{\epsilon}$  dependence follows from the canard theory (see e.g. [16, 17, 55]). If one of these estimates are violated then we still expect to observe MMO pattern but we cannot predict the exact MMO pattern. Theorem 4.2 in [17] covers the case where  $\delta$  violates this condition.

For example, Table I predicts for  $I_{app} = -2.4$  four secondary canards and therefore a maximal number  $s^* = 5$  of STOs. If we compare the prediction with Figure 2 (d) then we see that a  $1^3$  MMO patterns is realized with that particular choice of initial conditions. Therefore, Assumption 2 and/or 3 is violated, i.e.  $\mu$  and/or  $\delta$  are of order  $O(\sqrt{\epsilon})$  where  $\sqrt{\epsilon} \sim 0.15$ . For  $I_{app} = -2.4$ , Table I shows that  $\mu \sim 0.1$  and we estimate from Figure 9 (a) that  $\delta \sim 0.02$ . Hence, both parameters are within the order  $O(\sqrt{\epsilon})$  which explains why we do not find the maximal MMO pattern predicted by the singular perturbation theory. Nonetheless, we can explain certain trends. For instance, if we increase  $\delta$ , i.e. if we decrease the initial conditions on  $S_a$  (to physiological irrelevant negative values), then we observe an increase in STOs until we reach a maximum value of STOs. In the case  $I_{app} = -2.4$ ,  $1^8$  MMO is the maximum pattern which is observed for initial conditions  $r_s < -0.12$  (data not shown). Clearly, the maximum number of STOs, although larger than predicted, is still finite and reflects therefore the characteristics of a folded node induced MMO pattern. The perturbation  $\epsilon$  is simply too large to give precise estimates on STOs. On the other hand, if we sufficiently decrease  $\epsilon$  then we should observe the maximal  $1^5$  pattern as predicted. In this case, any  $\epsilon < 10^{-5}$  gives this predicted result (data not shown).

Note that in the folded saddle-node limit  $\mu \rightarrow 0$  an unbounded growth of STOs is expected. Folded saddle-nodes are related to the transition from an excitable to an oscillatory state and we observe a large number of STOs in our simulations, e.g. for  $I_{app} = 2.55$  in Figure 2 (a). The MMO theory for this limiting case has still to be developed. So far, MMOs related to folded saddle-node singularities have been studied in [47] for a 3d-autocatalator problem and in [23] for a dopaminergic neuron model.

### **I. Dependence of the subthreshold oscillatory frequency on the amount of the h-current**

The dynamic picture described in Section IV F is qualitatively affected by changes in the amount of the h-current, measured by the parameter  $G_h$ . We now consider values of  $G_h$  lower than the one considered in Section IV F. The following table shows that the ranges of values

Dimensional			Dimensionless		
$G_h$	folded nodes for	interval size	$G_h$	folded nodes for	interval size
1.5	$-2.64 < I_{app} < -1.86$	0.78	1.0	$-0.0176 < I_{app} < -0.0124$	0.0052
1.4	$-2.43 < I_{app} < -1.72$	0.71	0.933	$-0.0162 < I_{app} < -0.0115$	0.0047
1.3	$-2.21 < I_{app} < -1.58$	0.63	0.866	$-0.0147 < I_{app} < -0.0105$	0.0042
1.2	$-1.98 < I_{app} < -1.43$	0.55	0.8	$-0.0132 < I_{app} \leq 0.0095$	0.0037
1.0	$-1.51 < I_{app} < -1.12$	0.39	0.666	$-0.0101 < I_{app} < -0.0075$	0.0026
0.5	$-0.24 < I_{app} < -0.11$	0.13	0.333	$-0.0016 < I_{app} < -0.0007$	0.0009

TABLE II: Folded node regimes for different  $G_h$  values.

of  $I_{app}$  for which the system (11)-(13) has a folded node shrink with increasing values of  $G_h$  and  $G_p = 0.5$  (dimensionless value:  $G_p = 0.3333$ ). Note that the decrease in the amount of  $I_h$  results in an increase of the amount of  $I_{app}$ .

Fig. 12 illustrates the effect that “balanced” changes in the values of  $G_h$  and  $I_{app}$  have on the MMO patterns for a constant value of  $G_p$ . To compensate for the decrease in the amount of  $I_h$  (decrease in  $G_h$ ) we increased  $I_{app}$  so that the number of STOs per spike is kept constant, and for a fixed value of  $G_h$ , a lower value of  $I_{app}$  would produce one less STO per spike. We observe that as we decrease  $G_h$  the STO frequency slightly decreases.

A decrease in the amount of  $I_h$  can be also compensated by an increase in the amount of  $I_p$ . In Figs. 13-a and -b the values of  $I_{app}$  are kept constant and the values of  $G_h$  and  $G_p$  were chosen following the principle described in the previous paragraph. Similarly to the previous case, as we decrease  $G_h$  the STO frequency slightly decreases.

### J. Inhibitory pulses decrease the number of subthreshold oscillations per spike and increase the SC firing frequency

Inhibitory pulses typically delay firing in the postsynaptic cell. However, this is partially reversed when the postsynaptic cell has a h-current [26, 56]. Heuristically, we expect a pulse of inhibition applied at different times  $t_{pert}$  to have a differential effect on the postsynaptic spike-time. When the pulse of inhibition is applied to a SC whose trajectory is still far away from the “rotational region”, it will have little effect, since the trajectory will have enough time to recover before starting to rotate. In contrast, a pulse of inhibition of the same magnitude applied to a SC that is already rotating may cause it to move from one rotational sector to another with a lower number of STOs or no STOs at all. As a consequence, the spike-time of

the perturbed SC will be considerably advanced with respect to the one of the unperturbed cell. We illustrate this in Figs. 14 and 15 for two different values of  $I_{app}$ . In Fig. 14, the unperturbed SC displays one STO per spike. The pulses of inhibition applied at  $t_{pert} = 2.66$  and  $t_{pert} = 2.83$  move the trajectory outside the funnel and cause the SC to spike with no STOs. In Fig. 15, the unperturbed SC has three STOs per spike. Pulses of inhibition applied at  $t_{pert} = 3.33$  and  $t_{pert} = 5.0$  move the trajectory to sectors corresponding to two and one STOs per spike respectively, and a pulse of inhibition applied at  $t_{pert} = 5.83$  moves the trajectory outside the funnel and causes the SC to spike with no STOs.

## V. DISCUSSION

Stellate cells (SCs) of the medial entorhinal cortex (MEC) display subthreshold oscillations (STOs) and mixed-mode oscillations (MMOs) at theta frequencies [8, 9]. In these MMO patterns, spikes occur at the peak of STOs, though not at every cycle. STOs found in single SCs are the result of the interaction between  $I_h$  and  $I_p$  [7–9]. It was recently found that their frequency varies along the dorsal-to-ventral axis of the MEC, scaling with the MEC grid-cells [3] that are believed to contain a neural map of the spatial environment [4–6].

Previous theoretical work has focused on various aspects of SC dynamics using biophysical (conductance based) models: Reproducing, via simulations, STOs, MMOs and fully spiking patterns [10, 12–14, 30], the computational study of resonant properties of SCs [14, 57], and the computational study of synchronization properties of networks including SCs. [10, 12, 26].

In [10] we initiated a more detailed mechanistic study of the generation of STOs and MMOs in the seven-dimensional SC model proposed in [12]. We considered there a rather restricted set of parameters. Using reduction of dimensions techniques we argued that this model can be approximated in the subthreshold regime by the three-dimensional fast-slow system (1)-(3) studied in this paper (the dimensional SC model), which accounts for the interactions between  $I_p$  and  $I_h$ . Using computational techniques and dynamical systems ideas we hypothesized that this interaction is intrinsically non-linear and that the generation of STOs and MMOs is governed by the three-dimensional canard phenomenon.

In this paper we used analytical and computational tools to show that the three-dimensional canard phenomenon is the main player in the mechanism of generation of STOs in the SC model (1)-(3) for a broad range of biophysically plausible parameter values that include these considered in [10]. The underlying dynamic structure also describes the onset of spikes, but not the spike dynamics. Once the oscillating trajectory escapes the subthreshold regime to the spiking one, the reset properties of the h-current provide the additional mechanism needed for the trajectory to return to the subthreshold regime and produce MMOs.

From the mathematical point of view, our results show that the SC model (1)-(3) satisfy the conditions required by the theorems proposed in [17] (see Section IV D) to guarantee the existence of MMOs. Thus, the SC model becomes a biologically plausible example of the theory developed in [17]. Care has to be taken in the limiting case of a folded saddle-node ( $\mu \rightarrow 0$ ) since the corresponding theory has still to be developed. Nonetheless, trends can be deduced from the folded node analysis and by sufficiently decreasing the singular perturbation parameter as shown in section IV H. Examples related to other phenomena include those studied in [16, 45].

From the mechanistic point of view, our results provide an analytical and geometric framework to study various dynamic aspects of SCs: The role that the participating currents and their interaction play in shaping the observed MMO patterns, some of the consequences of these interactions when SCs receive external inputs (sinusoidal or synaptic like) and the prediction of the effect that different amount of the participating currents may have on the observed MMO patterns. These differences could be due to a heterogeneous distribution of channels in the EC, to the effect of neuromodulators, or to changes due to development.

A very important component of the framework we refer to above is the singular funnel. By calculating the strong canard it is possible to make qualitative predictions about whether STOs are expected within the spiking pattern or not, i.e., which initial conditions in the subthreshold regime lead to MMOs and which lead to fully spiking patterns. One can be more explicit about the precise number of STOs by further calculating the secondary canards. Changes in the parameters of the model are reflected in the singular funnel via changes in the strong canard, changes in the secondary canards, or changes in the initial conditions in the subthreshold regime due to variations in the trajectory reset values. So, for example, the trajectory corresponding to a specific initial condition and a certain set of parameters may enter the funnel while the trajectory corresponding to the same initial conditions and a different set of parameters may be left outside. The tools required to make more accurate quantitative predictions call for further research.

The results of this paper support our previous hypothesis [10] of the existence of a canard geometric/dynamic structure as the main player in the mechanism of generation of STOs in SCs. This canard structure is generated by the (nonlinear) nullsurfaces and the time scale separation between the participating variables, and it has the potential of producing the canard phenomenon. More specifically, STOs in SCs have been proposed to be sustained by a “push-pull” interplay between  $I_p$  and  $I_h$  [7, 8]. In particular,  $I_h$  has been proposed to play a major pacemaker role in the generation of STOs providing a delayed feedback mechanism to the voltage changes led by  $I_p$ . This mechanism depends on the dynamic (kinetic) properties of  $I_h$ . There are various players in this interaction: The amount of  $I_h$  and  $I_p$  (expressed by the

maximal conductances  $G_h$  and  $G_p$ ), the relative speeds of the voltage and gating variables, and the nonlinearities associated with the dynamic equations. Our results show that these are encoded in the canard structure. Different sets of parameters lead to similar canard structures which produce similar voltage traces: In our model, a decrease in  $G_h$  (reflecting a decrease in the amount of  $I_h$ ) leads to an increase in the “height” of the  $v$ -nullsurface. Since the other nullsurfaces do not depend on the parameter of the model, for fixed values of  $I_{app}$  and low enough value of  $G_h$ , folded nodes no longer exists and trajectories will be attracted to a stable fixed-point (see Table in Section IV I). However, this can be reversed by increasing the value of  $I_{app}$ , which lowers the  $V$ -nullsurface. The facts that MMOs with the same number of STOs per spike with roughly the same amplitude are obtained for different pairs of  $(G_h, I_{app})$  and  $(G_h, G_p)$  (see Figs. 12 and 13) shows that it is not a specific property of  $I_h$  and  $I_p$  that creates the STOs but rather a property of the various appropriate balances these currents can create, which are reflected in the generation of similar or “equivalent” canard structures. This raises the question of whether internal homeostatic mechanisms exist that keep the number of STOs per spike unchanged. On the other hand, as we mentioned earlier, the fact that the STO frequency changes with  $I_h$  shows a way in which the canard mechanism can account for the difference in frequencies experimentally observed in SCs along the ventral-to-dorsal axis of the entorhinal cortex [3].

Spike-time response curves (STRCs) techniques have been used to study the synchronization properties of small networks including SCs [12, 25, 26], in particular to investigate how synchronization depends on key ionic currents known to be important to the theta rhythm. STRCs are functions that measure the effect of a spike of a presynaptic cell on the timing of the next spike of the postsynaptic cell. (STRCs are essentially the same as phase response curves [58, 59].) Our results also support the hypothesis of the canard structure as an important component in the mechanism of synchronization in networks including SCs and other excitatory and inhibitory neurons.

There has been some controversy in the literature about whether the observed subthreshold oscillations in SCs are intrinsically linear or nonlinear phenomena [14, 57]. As predicted in [10], our results show that the latter is the most plausible case. Our results also show that the interaction between  $I_p$  and  $I_h$  responsible for the generation of STOs involves both components of  $I_h$ , not only the fast one; i.e., the slow component of  $I_h$  does not simply play a modulatory role in the generation of STOs, but rather a dynamic one.

As it occurs for many conductance-based models, the concept of spiking threshold is not well defined in the SC model we study here (see [60] for a discussion on the topic). There are two ways in which spikes are generated in the SC model, leading to patterns whose interspike intervals differ roughly by an order of magnitude. The first type corresponds to initial

conditions such that the trajectory is “captured” by the slow manifold  $S$ . The spiking period between two such spikes is determined by the time it takes the trajectory to move along the slow manifold. These trajectories may or may not enter the funnel. In either case, the onset of spikes occurs when the trajectory moves away from the slow manifold along a fast fiber towards the spiking regime. Once this occurs, spiking is unavoidable; i.e., the trajectory does not have to cross any voltage threshold value to spike. In the nonlinear artificially spiking model, the value of  $v_{th}$  only indicates that a spike has occurred so it can be (artificially) added to the voltage trace. The second type of spike corresponds to initial conditions such that the trajectory is never “captured” by the slow manifold  $S$ . These initial conditions are above the fold-curve. The period between two such spikes is determined by the time it takes the trajectory to move along a fast fiber (vertical direction); i.e., its order of magnitude is  $\epsilon$ . As for the first type, once the trajectory enters the subthreshold regime a spike will occur without the need of a voltage threshold value. Spontaneous spikes of the second type are expected to be rare, since reset voltage values are typically lower than the one corresponding to the fold-curve. However, trajectories may be forced to change from one spiking regime to the other by external inputs. This may have consequences for network dynamics in the entorhinal cortex.

There are several aspects of the SC dynamics not studied in this paper. One of them is how noise affects the MMO patterns. One important source of noise is the set of persistent sodium channels [13, 61]. In [10] we showed that STOs are less regular and more robust when persistent sodium channel noise is added to the SC model studied here. A second aspect is spike clustering, where two or more spikes occur without interspersed STOs. Noisy MMOs and clustering have been reproduced via simulations in the biophysical (conductance-based) model presented in [13]. Whether or not this model has an underlying canard structure qualitatively similar to the one we uncovered in this paper is still an open question.

### Acknowledgments

We thank Tasso Kaper for his useful comments on an earlier draft of this manuscript, and Amit Bose, Morten Brøns, Martin Krupa and John White for discussions.

- 
- [1] D. Johnston and D. G. Amaral. Hippocampus. *In The Synaptic Organization of the Brain*, G. M. Sheperd, ed. (Oxford University Press), pages 455–498, 2004.

- [2] H. E. Scharfman, M. P. Witter, and R. Schwarcz. *The Parahippocampal region: Implications for neurological and psychiatric diseases*. Annals of the New York Academy of Sciences, V. 911, 2000.
- [3] L. M. Giacomo, E. A. Zilli, E. Fransén, and M. E. Hasselmo. Temporal frequency of subthreshold oscillations scales with entorhinal grid cell field spacing. *Science*, 315:1719–1722, 2007.
- [4] M. Fyhn, S. Molden, M. P. Witter, Moser E. I., and M. B. Moser. Spatial representation in the entorhinal cortex. *Science*, 305:1258–1264, 2004.
- [5] T. Hafting, M. Fyhn, S. Molden, M. B. Moser, and E. I. Moser. Microstructure of a spatial map in the entorhinal cortex. *Nature*, 436:801–806, 2005.
- [6] F. Sargolini, M. Fyhn, T. Hafting, B. McNaughton, M. P. Witter, E. I. Moser, and M. B. Moser. Conjunctive representation of position, direction, and velocity in the entorhinal cortex. *Science*, 312:758–762, 2006.
- [7] C. T. Dickson, J. Magistretti, M. H. Shalinsky, E. Fransén, M. Hasselmo, and A. A. Alonso. Properties and role of  $I_h$  in the pacing of subthreshold oscillation in entorhinal cortex layer II neurons. *J. Neurophysiol.*, 83:2562–2579, 2000.
- [8] A. A. Alonso and R. R. Llinás. Subthreshold  $\text{Na}^+$ -dependent theta like rhythmicity in stellate cells of entorhinal cortex layer II. *Nature*, 342:175–177, 1989.
- [9] C. T. Dickson, J. Magistretti, M. Shalinsky, B. Hamam, and A. A. Alonso. Oscillatory activity in entorhinal neurons and circuits. *Ann. N.Y. Acad. Sci.*, 911:127–150, 2000.
- [10] H. G. Rotstein, T. Oppermann, J. A. White, and N. Kopell. A reduced model for medial entorhinal cortex stellate cells: subthreshold oscillations, spiking and synchronization. *Journal of Computational Neuroscience*, 21:271–292, 2006.
- [11] A. A. Alonso and E. García Austt. Neuronal sources of theta rhythm in the entorhinal cortex of the rat. II. phase relations between unit discharges and theta field potentials. *Exp. Brain Res.*, 67:493–501, 1987.
- [12] C. D. Acker, N. Kopell, and J. A. White. Synchronization of strongly coupled excitatory neurons: relating network behavior to biophysics. *Journal of Computational Neuroscience*, 15:71–90, 2003.
- [13] E. Fransén, A. A. Alonso, C. T. Dickson, and M. E. Magistretti, J. Hasselmo. Ionic mechanisms in the generation of subthreshold oscillations and action potential clustering in entorhinal layer II stellate neurons. *Hippocampus*, 14:368–384, 2004.
- [14] S. Schreiber, I. Erchova, U. Heinemann, and A. V. Herz. Subthreshold resonance explains the frequency-dependent integration of periodic as well as random stimuli in the entorhinal cortex. *J. Neurophysiol.*, 92:408–415, 2004.
- [15] P. Szmolyan and M. Wechselberger. Canards in  $R^3$ . *J. Diff. Eq.*, 177:419–453, 2001.
- [16] M. Wechselberger. Existence and bifurcation of canards in  $R^3$  in the case of a folded node.

- SIAM J. Appl. Dyn. Syst.*, 4:101–139, 2005.
- [17] M. Brøns, M. Krupa, and M. Wechselberger. Mixed mode oscillations due to the generalized canard phenomenon. *Fields Institute Communications*, 49:39–63, 2006.
- [18] R. Larter and C. G. Steinmetz. Chaos via mixed mode oscillations. *Philos. Trans. R. Soc. London A*, 337:291–298, 1991.
- [19] A. Arneado, F. Argoul, J. Elezgaray, and P. Richetti. Homoclinic chaos in chemical systems. *Physica D*, 62:134–168, 1993.
- [20] N. Kopell. Toward a theory of modelling central pattern generators. In A. H. Cohen, S. Rossignol, S. Grillner, eds. *Neural Control of Rhythmic Movements in Vertebrates*. Wiley, New York., pages 369–413, 1988.
- [21] J. Guckenheimer, R. Harris-Warrick, Peck J., and A. Willms. Bifurcation, bursting and spike frequency adaptation. *Journal of Computational Neuroscience*, 4:257–277, 1997.
- [22] J. Guckenheimer and A. R. Willms. Asymptotic analysis of subcritical Hopf-homoclinic bifurcation. *Physica D*, 139:159–216, 2000.
- [23] M. Krupa, N. Popovic, N. Kopell, and H. G. Rotstein. Mixed-mode oscillations in a three time-scale model for the dopaminergic neuron. 18:015106, 2008.
- [24] M. Brøns, T. J. Kaper, and H. G. Rotstein. Introduction to focus issue: Mixed mode oscillations: Experiment, computation, and analysis. 18:015101, 2008.
- [25] T. I. Netoff, M. I. Banks, A. D. Dorval, C. D. Acker, J. S. Haas, N. Kopell, and J. A. White. Synchronization in hybrid neuronal networks of the hippocampal formation. *J. Neurophysiol.*, 93:1197–1208, 2005.
- [26] D. D Pervouchine, T. I. Netoff, H. G. Rotstein, J. A. White, M. O. Cunningham, M. A. Whittington, and N. Kopell. Low-dimensional maps encoding dynamics in entorhinal cortex and hippocampus. *Neural Computation*, 18:2617–2650, 2006.
- [27] D. Johnston and S. M.-S. Wu. *Foundations of cellular neurophysiology*. The MIT Press, Cambridge, Massachusetts, 1995.
- [28] R. M. Klink and A. A. Alonso. Ionic mechanisms of muscarinic depolarization in entorhinal cortex layer II neurons. *J. Neurophysiol.*, 77:1829–1843, 1997.
- [29] J. Magistretti and A. A. Alonso. Biophysical properties and slow voltage-dependent inactivation of a sustained sodium current in entorhinal cortex layer-II principal neurons. a whole-cell and single-channel study. *J. Gen. Physiol.*, 114(4):491–509, 1999.
- [30] E. Fransén, C. T. Dickson, J. Magistretti, A. A. Alonso, and M. E. Hasselmo. Modeling the generation of subthreshold membrane potential oscillations of entorhinal cortex layer II stellate cells. *Soc Neurosci. Abstr.*, 24:814.815, 1998.
- [31] E. Fransén, G. V. Wallestein, A. A. Alonso, C. T. Dickson, and M. E. Hasselmo. A biophysical

- simulation of intrinsic and network properties of entorhinal cortex. *Neurocomputing*, 26-27:375–380, 1999.
- [32] R. B. Robinson and S. A. Siegelbaum. Hyperpolarization-activated cation currents: from molecules to physiological function. *Annu. Rev. Physiol.*, 65:453–480, 2003.
- [33] B. Hutcheon and Y. Yarom. Resonance oscillations and the intrinsic frequency preferences in neurons. *Trends in Pharmacological Sciences*, 23:216–222, 2000.
- [34] M. J. E. Richardson, N. Brunel, and V. Hakim. From subthreshold to firing-rate resonance. *J. Neurophysiol.*, 89:2538–2554, 2003.
- [35] E. M. Izhikevich. Resonate-and-fire neurons. *Neural Networks*, 14:883–894, 2001.
- [36] M. Wechselberger. Canards. *Scholarpedia*, 2(4):1356, 2007.
- [37] E. Benoit, J. L. Callot, F Diener, and Diener M. *Chasse au Canard*. IRMA, Strasbourg, 1980.
- [38] W. Eckhaus. Relaxation oscillations including a standard chase on french ducks. *In Lecture Notes in Mathematics, Springer-Verlag*, 985:449–497, 1983.
- [39] F. Dumortier and R. Roussarie. Canard cycles and center manifolds. *Memoirs of the American Mathematical Society*, 121 (577), 1996.
- [40] M. Krupa and P. Szmolyan. Relaxation oscillation and canard explosion. *J. Diff. Eq.*, 174:312–368, 2001.
- [41] M. Brøns and K. Bar-Eli. Canard explosion and excitacion in a model of the Belousov-Zhabotinsky reaction. *J. Phys. Chem.*, 95:8706–8713, 1991.
- [42] B. Peng, V. Gaspar, and K. Showalter. False bifurcations in chemical systems: Canards. *Philos. Trans. R. Soc. London A*, 337:275–289, 1991.
- [43] V. A. Makarov, V. I. Nekorkin, and M. G. Velarde. Spiking behavior in a noise-driven system combining oscillatory and excitatory properties. *Phys. Rev. Lett.*, 15:3031–3034, 2001.
- [44] C. B. Muratov and E. Vanden-Eijnden. Noise-induced mixed-mode oscillations in a relaxation oscillator near the onset of a limit cycle. 18:015111, 2008.
- [45] J. Rubin and M. Wechselberger. Giant squid - hidden canard: the 3d geometry of the hodgkin-huxley model. *Biol. Cybern.*, 97:5–32, 2007.
- [46] A. Milik and P. Szmolyan. Multiple time scales and canards in a chemical oscillator. *in Multiple Time-Scale Dynamical systems (IMA Volume) edited by C. K. R. T. Jones and A. Khibnik (Springer - New York)*, 122, 2000.
- [47] A. Milik, P. Szmolyan, H. Löffelmann, and E. Groller. Geometry of mixed-mode oscillations in the 3d-autocatalator. *Int. J. Bif. Chaos*, 8:505–519, 1998.
- [48] J. Drover, J. Rubin, J. Su, and B. Ermentrout. Analysis of a canard mechanism by which excitatory synaptic coupling can synchronize neurons at low firing frequencies. *SIAM J. Appl. Math.*, 65:69–92, 2004.

- [49] L. P. Shilnikov. A case of the existence of a denumerable set of periodic motions. *Sov. Math. Dokl.*, 6:163–166, 1965.
- [50] H. Richter, R. Klee, U. Heinemann, and Eder C. Developmental changes of inward rectifier currents in neurons of the rat entorhinal cortex. *Neuroscience Letters*, 228:139–141, 1997.
- [51] N. Fenichel. Persistence and smoothness of invariant manifolds for flows. *Ind. Univ. Math. J.*, 21:193–225, 1971.
- [52] C. K. R. T. Jones. Geometric singular perturbation theory. *Lecture Notes in Mathematics*, 1609:44–118, 1994.
- [53] G. B. Ermentrout. *Simulating, analyzing, and animating dynamical systems. A guide to XPPAUT for researchers and students*. Society for Industrial and Applied Mathematics (Philadelphia, PA, USA), 2002.
- [54] R. L. Burden and J. D. Faires. *Numerical analysis*. PWS Publishing Company - Boston, 1980.
- [55] M. Wechselberger and W. Weckesser. Bifurcations of mixed-mode oscillations in a stellate cell model. *preprint*, 2008.
- [56] H. G. Rotstein, N. Kopell, A. Zhabotinsky, and I. R. Epstein. A canard mechanism for localization in systems of globally coupled oscillators. *SIAM J. Appl. Math.*, 63:1998–2019, 2003.
- [57] J. S. Haas and White. J. A. Frequency selectivity of layer II stellate cells in the medial entorhinal cortex. *J. Neurophysiol.*, 88:2422–2429, 2002.
- [58] J. Winson. Loss of hippocampal theta rhythm results in spatial memory deficit in the rat. *Science*, 201:160–163, 1978.
- [59] G. B. Ermentrout, M. Pascal, and B. Gutkin. The effects of spike frequency adaptation and negative feedback on the synchronization of neural oscillators. *Neural Computat.*, 13:1285–1310, 2001.
- [60] E. Izhikevich. *Dynamical Systems in Neuroscience: The geometry of excitability and bursting*. MIT Press (Cambridge, Massachusetts), 2006.
- [61] J. A. White, R. Klink, A. Alonso, and A. R. A. Kay. Noise from voltage-gated ion channels may influence neuronal dynamics in the entorhinal cortex. *J. Neurophysiol.*, 80:262–269, 1998.

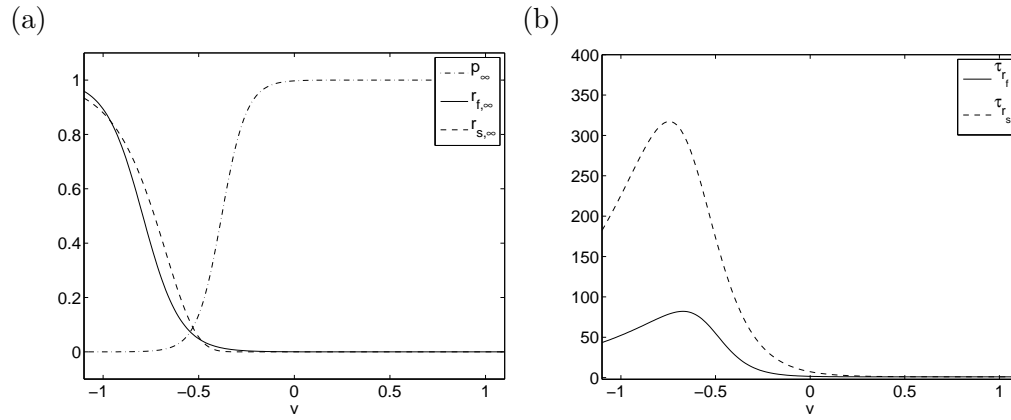


FIG. 1: SC model (1)-(3). **(a)** Activation/inactivation curves:  $p_\infty(v)$ ,  $r_{f,\infty}(v)$  and  $r_{s,\infty}(v)$ . **(b)** Voltage-dependent time scales:  $\tau_{rf}(v)$  and  $\tau_{rs}(v)$ . The dimensionless voltage  $v$  is the result of the rescaling  $v = V/K_v$  with  $K_v = 100$  mV.

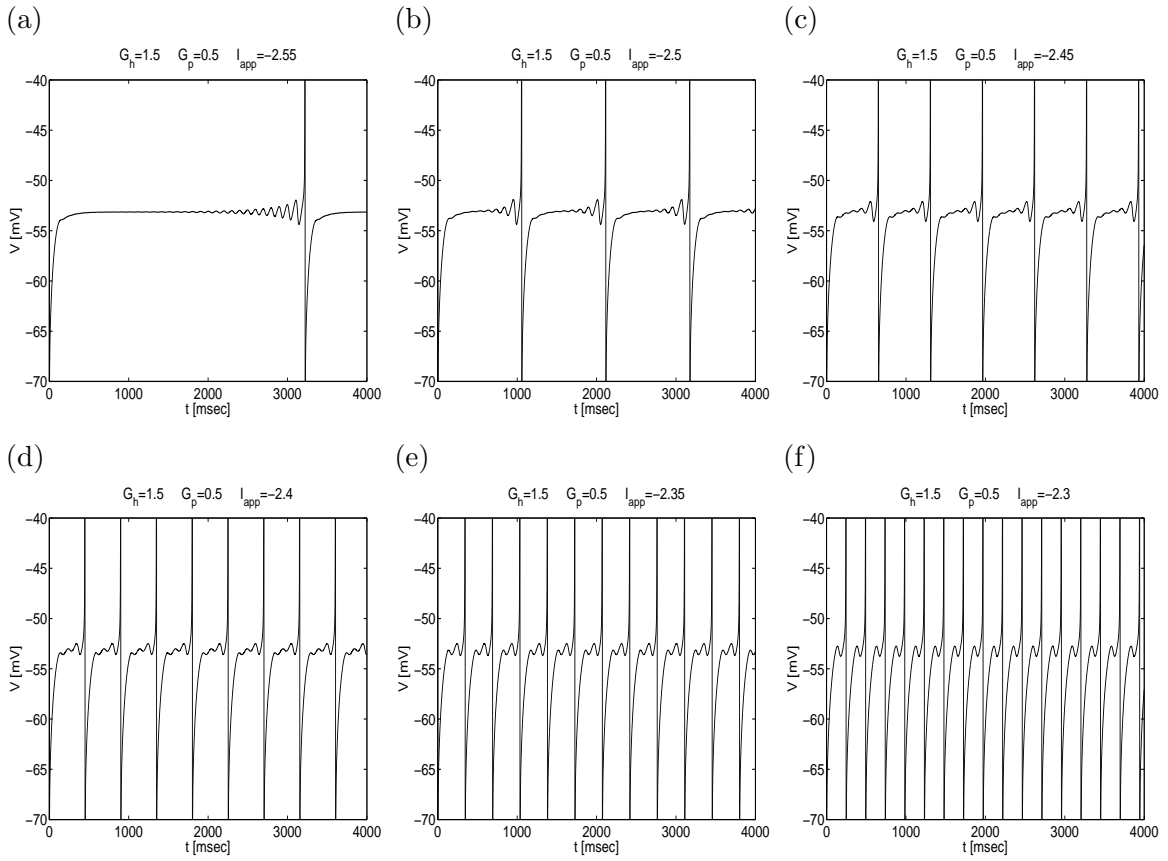


FIG. 2: Mixed-mode oscillatory patterns for the dimensional SC model (1)-(3) with  $V_{th} = -40$  mV and  $V_{rst} = -80$  mV. The number of subthreshold oscillations per spike decreases with increasing values of  $I_{app}$ . Note that  $V_{th}$  only indicates that a spike occurs and is not part of the mechanism of spike generation.

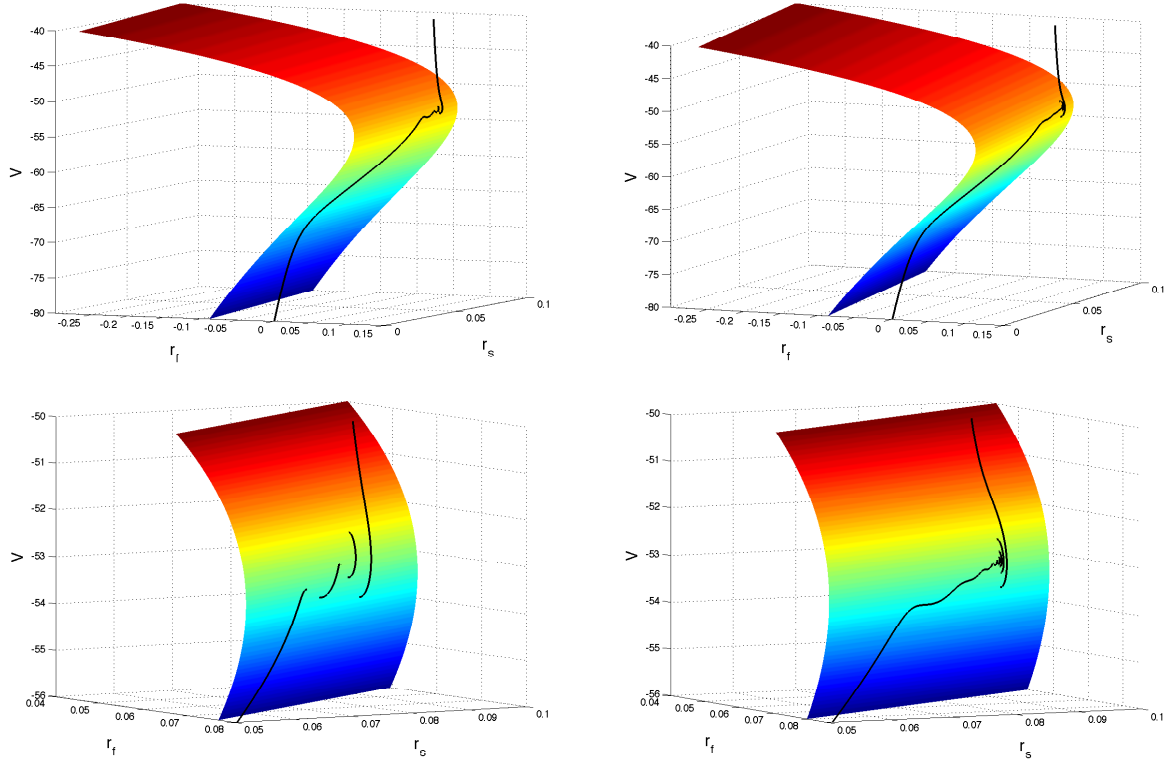


FIG. 3: Phase-space diagrams for the dimensional SC model (1)-(3);  $I_{app} = -2.4$  (left) and  $I_{app} = -2.5$  (right). The folded v-nullsurface is shown as well as the trajectories corresponding to the time traces shown in Figure 2 (d) and (b). Note, the trajectories evolve approximately along the v-nullsurface towards the fold-curve where they start to create subthreshold oscillations before they escape this regime to fire an action potential.

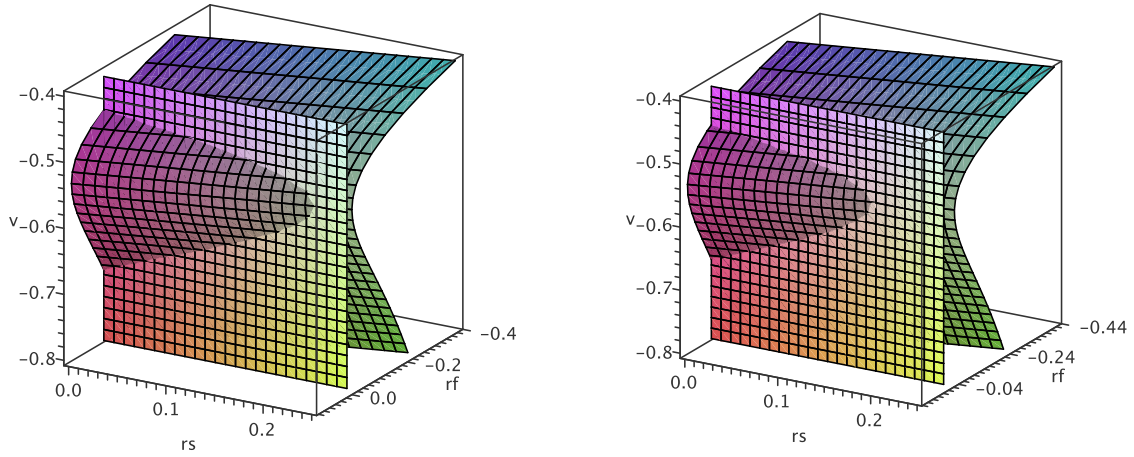


FIG. 4: Domains of possible initial conditions on the critical manifolds  $S$  for trajectories starting at the SC reset values. The left and right panels correspond to  $I_{app} = -2.64$  ( $-0.0176$ ) and  $I_{app} = -1.86$  ( $-0.0124$ ) respectively. The dimensionless values of the parameters are given in parenthesis. All panels correspond to  $G_h = 1.5$  ( $1.0$ ). This Figure illustrates the facts that  $I_{app}$  does not change the geometry of the critical manifold significantly and that  $I_{app}$  has also no significant influence on the domain of (biologically relevant) initial conditions.

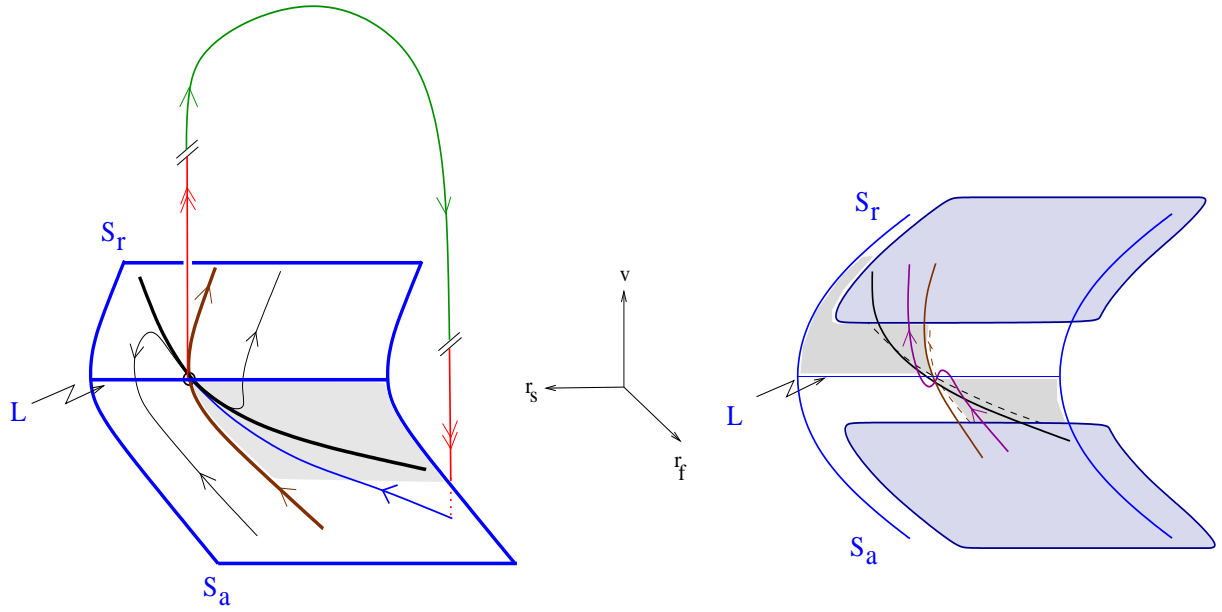


FIG. 5: Schematic representation of the ‘canard’ mechanism generating mixed-mode oscillations in the SC and related models: A folded node singularity, located on the fold-curve  $L$ , forms a singular funnel. A singular periodic orbit which consists of a segment on the attracting manifold  $S_a$  (blue) within the funnel with the folded node singularity as an endpoint. Then it follows a fast fiber of the layer problem (red) and a global return mechanism (green) projects the singular orbit back into the singular funnel. The return mechanism for the SC model is based on the reset properties of the h-current after a spike has occurred. The right panel shows a schematic representation of a trajectory rotating around the weak canard within the singular funnel.

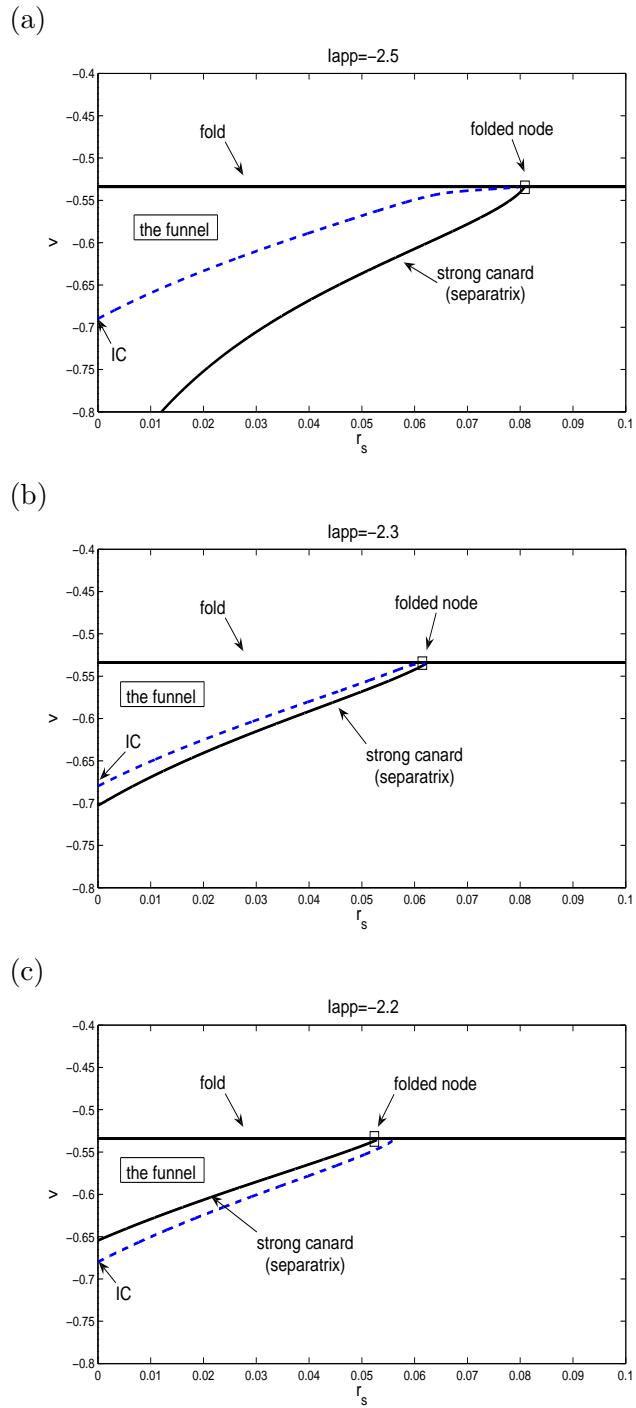


FIG. 6: Schematic representations of the singular funnel for various values of  $I_{app}$  and for  $G_h = 1.5$  (1.0) and  $G_p = 0.5$  (0.3333). The dimensionless values of the parameters are given in parenthesis. The singular funnel is bounded by the fold (horizontal) line and the strong canard. The funnel is located on the attracting part of the slow manifold  $S_a$  (below the fold). Trajectories (dashed lines) start at their initial conditions (IC) on the slow manifold and evolve towards the folded node.

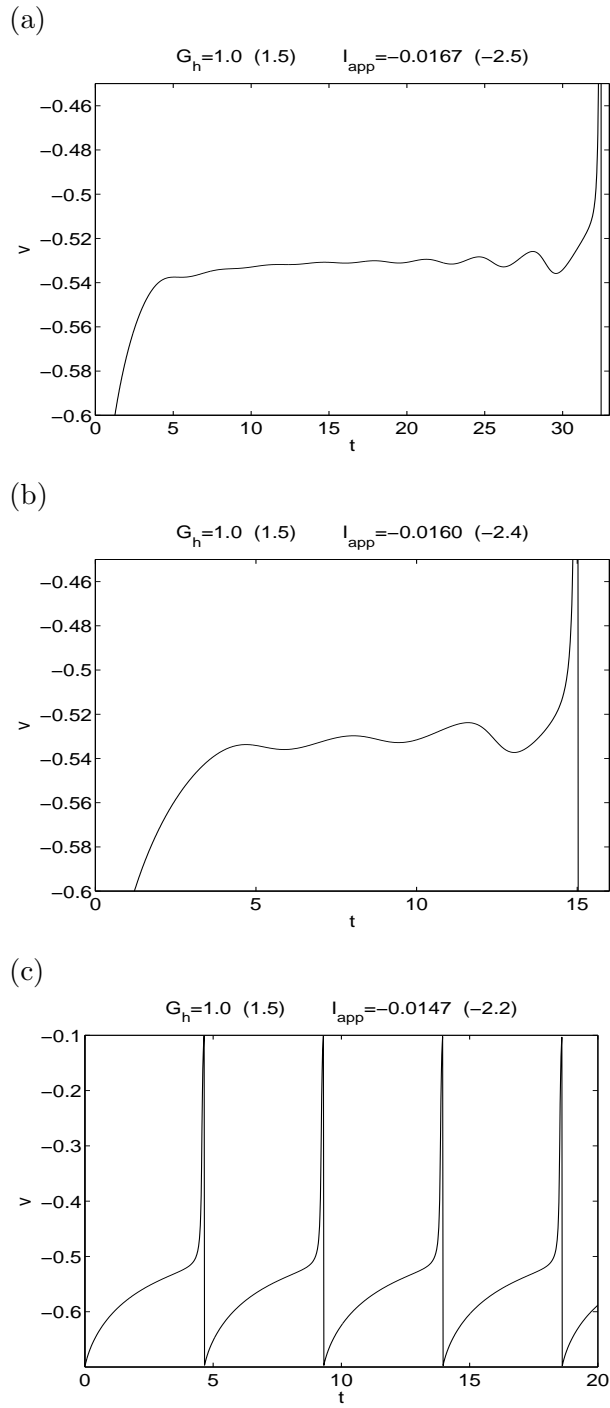


FIG. 7: Voltage traces for the (dimensionless) SC model (11)-(13).  $G_h = 0.5$  (0.3333). The dimensional values of  $G_h$  and  $I_{app}$  are given in parenthesis. The initial conditions correspond are located on the slow manifold  $S$ . The number of subthreshold oscillations per spike increases with decreasing values of  $I_{app}$ .

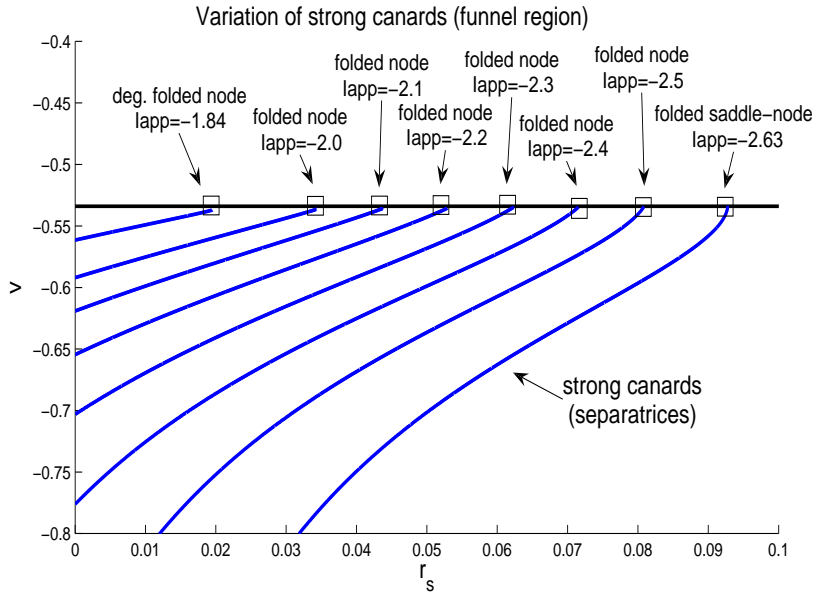


FIG. 8: Schematic representations of the singular funnel for various values of  $I_{app}$  and for  $G_h = 1.5$  (1.0) and  $G_p = 0.5$  (0.3333). The dimensionless values of the parameters are given in parenthesis. Each singular funnel is bounded by the fold (horizontal) line and the corresponding strong canard. The funnels are located on the attracting part of the slow manifold  $S_a$  (below the fold).

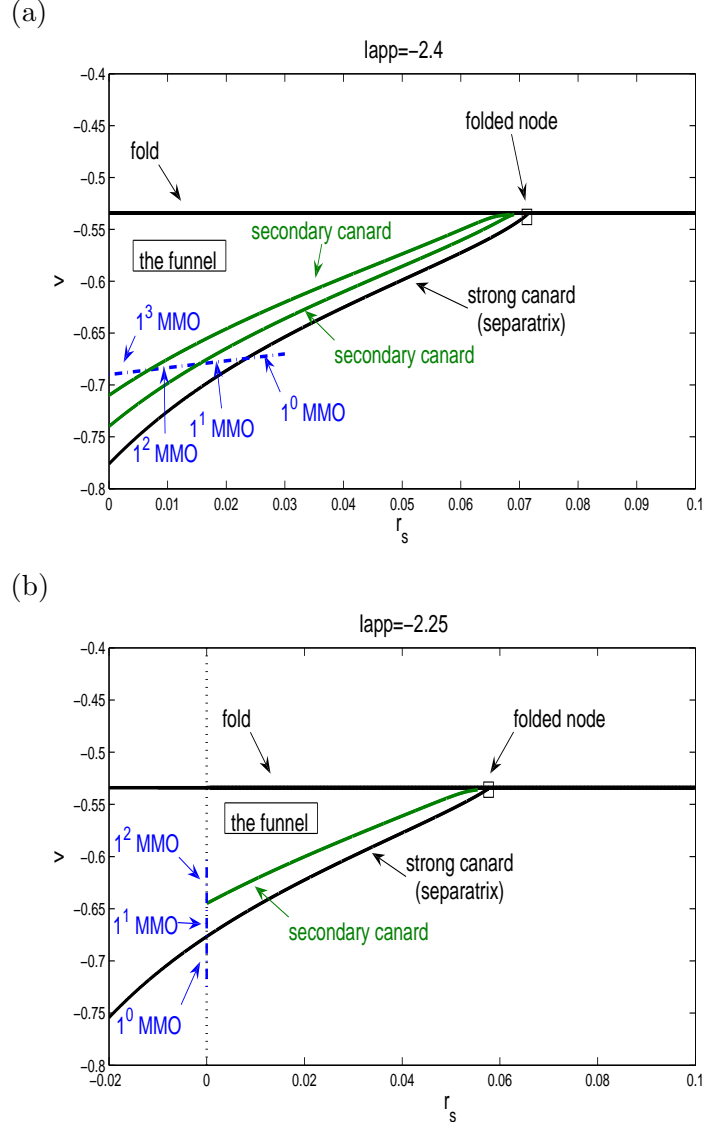


FIG. 9: Schematic illustration of the effect of changes in the initial values of the h-current gating variables  $r_s$  and  $r_f$  on the mixed-mode oscillatory patterns for  $G_h = 1.5$  (1.0),  $G_p = 0.5$  (0.3333) and (a)  $I_{app} = -2.4$  (-0.0160), and (b)  $I_{app} = -2.25$  (-0.0150). Each singular funnel is bounded by the “fold” line and the strong canard. The funnel is located on the attracting part of the slow manifold  $S_a$  (the repelling manifolds  $S_r$  are not shown). The secondary canards divide the funnel into sectors. Each sector corresponds to a  $1^s$  mixed mode oscillatory pattern. Trajectories starting in a given sector display  $s$  subthreshold oscillations per spike. Panel (a) corresponds to changes in  $r_s(0)$  for fixed values of  $v(0)$  and  $r_f(0)$ . The number of subthreshold oscillations per spike,  $s$ , decreases from left to right. The corresponding voltage traces are shown in Fig. 10. Panel (b) corresponds to changes in  $r_f(0)$  for fixed values of  $v(0)$  and  $r_s(0)$ . The number of subthreshold oscillations per spike,  $s$ , decreases from top to bottom. The corresponding voltage traces are shown in Fig. 11.

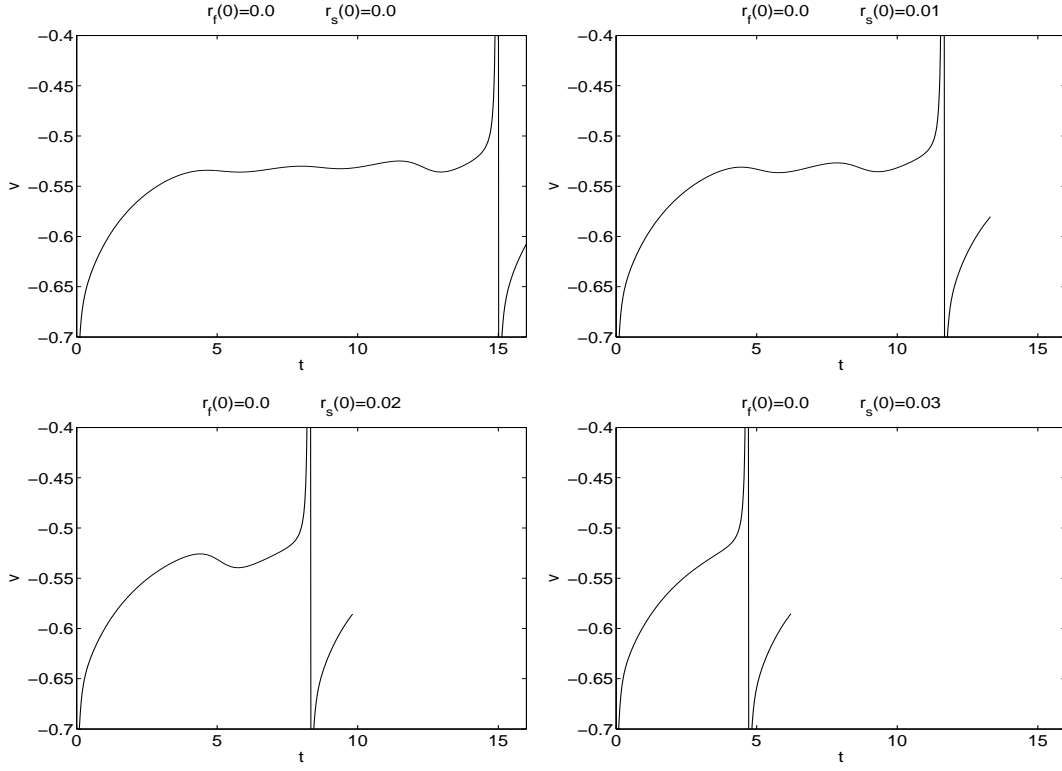


FIG. 10: Voltage traces showing the effect of changes in the initial values of  $r_s$  on the mixed-mode oscillatory patterns corresponding to trajectories starting in a vicinity of the slow manifold for fixed initial values of  $r_f$ . The dimensionless values of the parameters are given in parenthesis:  $G_h = 1.5$  (1.0),  $G_p = 0.5$  (0.3333),  $I_{app} = -2.4$  (-0.0160). The schematic representation of the corresponding singular funnel is given in Fig. 9-a.

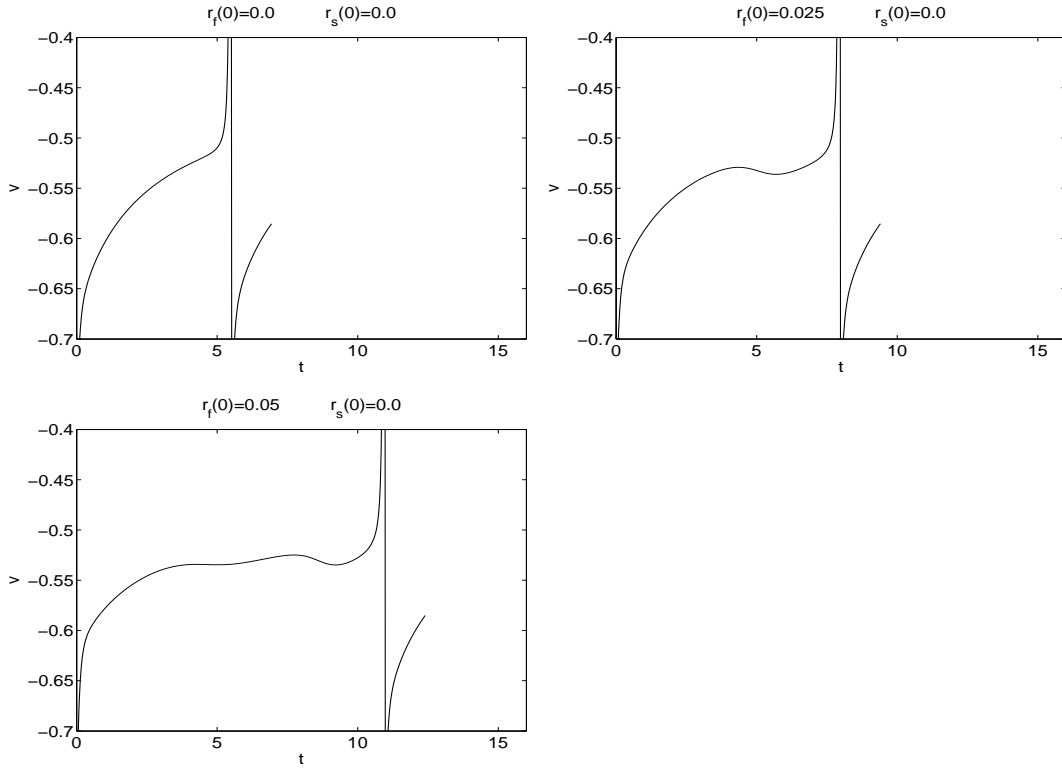


FIG. 11: Voltage traces showing the effect of changes in the initial values of  $r_f$  on the mixed-mode oscillatory patterns corresponding to trajectories starting in a vicinity of the slow manifold for fixed initial values of  $r_s$ . The dimensionless values of the parameters are given in parenthesis:  $G_h = 1.5$  (1.0),  $G_p = 0.5$  (0.3333),  $I_{app} = -2.25$  (-0.0150). The schematic representation of the corresponding singular funnel is given in Fig. 9-b.

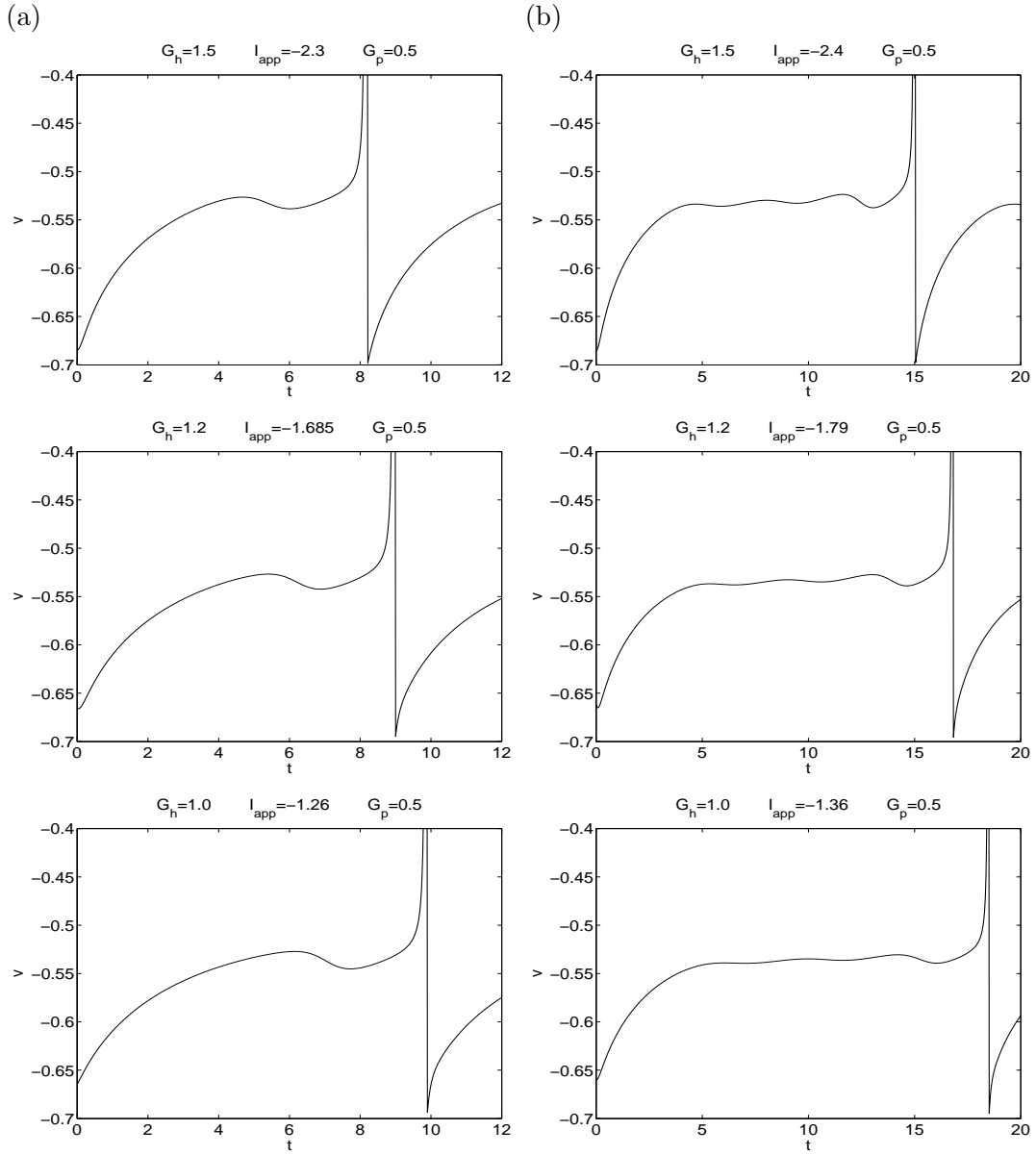


FIG. 12: Voltage traces showing the effect of changes in the values of  $G_h$  and  $I_{app}$  on the mixed-mode oscillatory patterns corresponding to trajectories starting in a vicinity of the slow manifold. The dimensionless values of the parameters are given in parenthesis.  $G_p = 0.5$  (0.3333). Top panel:  $G_h = 1.5$  (1.0) and (a)  $I_{app} = -2.3$  (-0.0153), (b)  $I_{app} = -2.4$  (-0.0160). Middle panel:  $G_h = 1.2$  (0.8) and (a)  $I_{app} = -1.685$  (-0.0112), (b)  $I_{app} = -1.79$  (-0.0119). Bottom panel:  $G_h = 1.0$  (0.6667) and (a)  $I_{app} = -1.26$  (-0.0084), (b)  $I_{app} = -1.36$  (-0.0091).

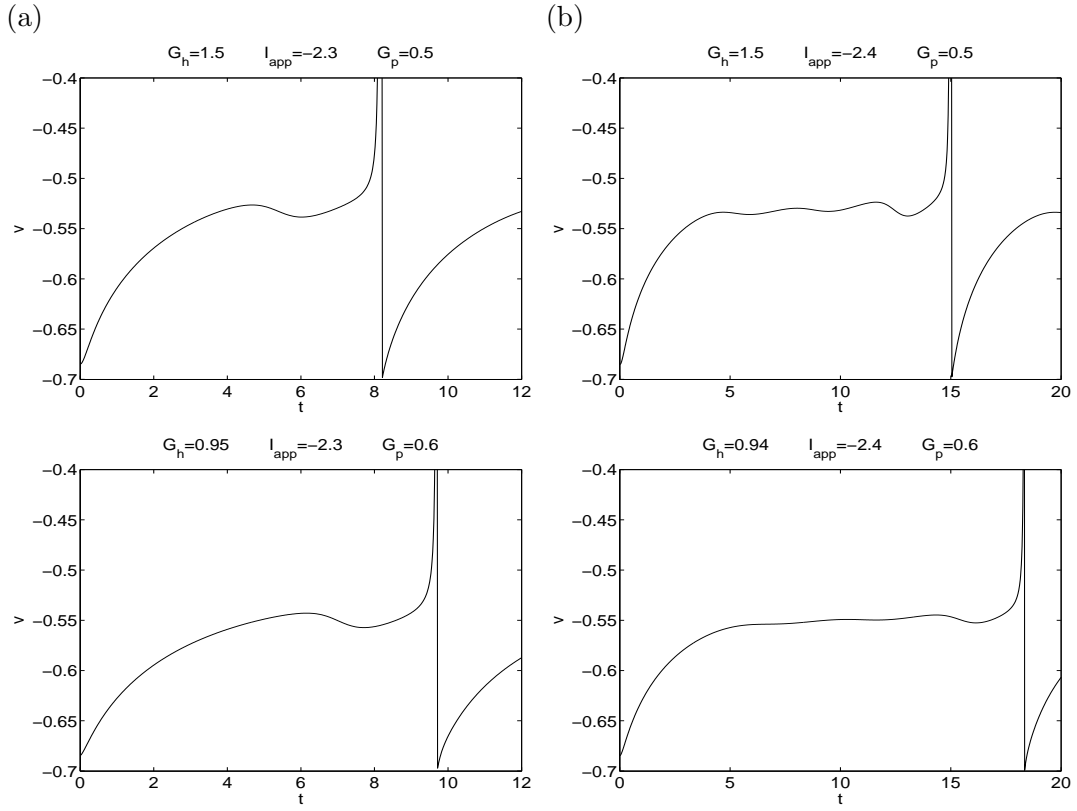


FIG. 13: Voltage traces showing the effects of changes in the value of  $G_h$  and  $G_p$  on the mixed-mode oscillatory patterns corresponding to trajectories starting in a vicinity of the slow manifold. The dimensionless values of the parameters are given in parenthesis. (a)  $I_{app} = -2.3$  (-0.0153) and (b)  $I_{app} = -2.4$  (-0.0160). Top panel:  $G_h = 1.5$  (1.0) and  $G_p = 0.5$  (0.3333), Bottom panel:  $G_p = 0.6$  (0.4) and (a)  $G_h = 0.95$  (0.6333) and (b)  $G_h = 0.94$  (0.6267).

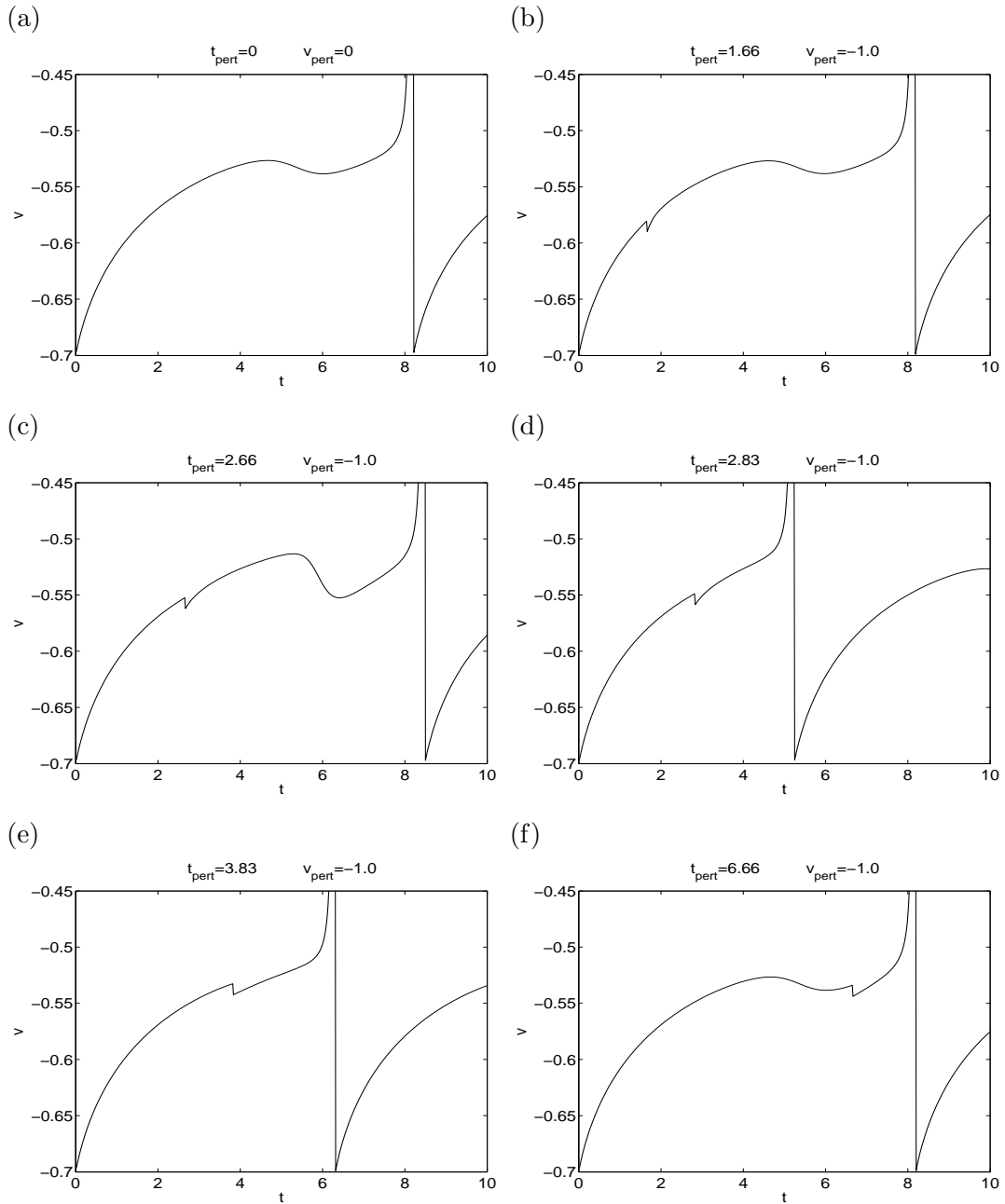


FIG. 14: Voltage traces showing the effect of inhibitory perturbations at various times  $t_{pert}$  on the mixed-mode oscillatory patterns corresponding to trajectories starting in a vicinity of the slow manifold for  $G_h = 1.5$  (1.0),  $I_{app} = -2.3$  ( $-0.0153$ ). The dimensionless values of  $G_h$  and  $I_{app}$  are given in parenthesis.

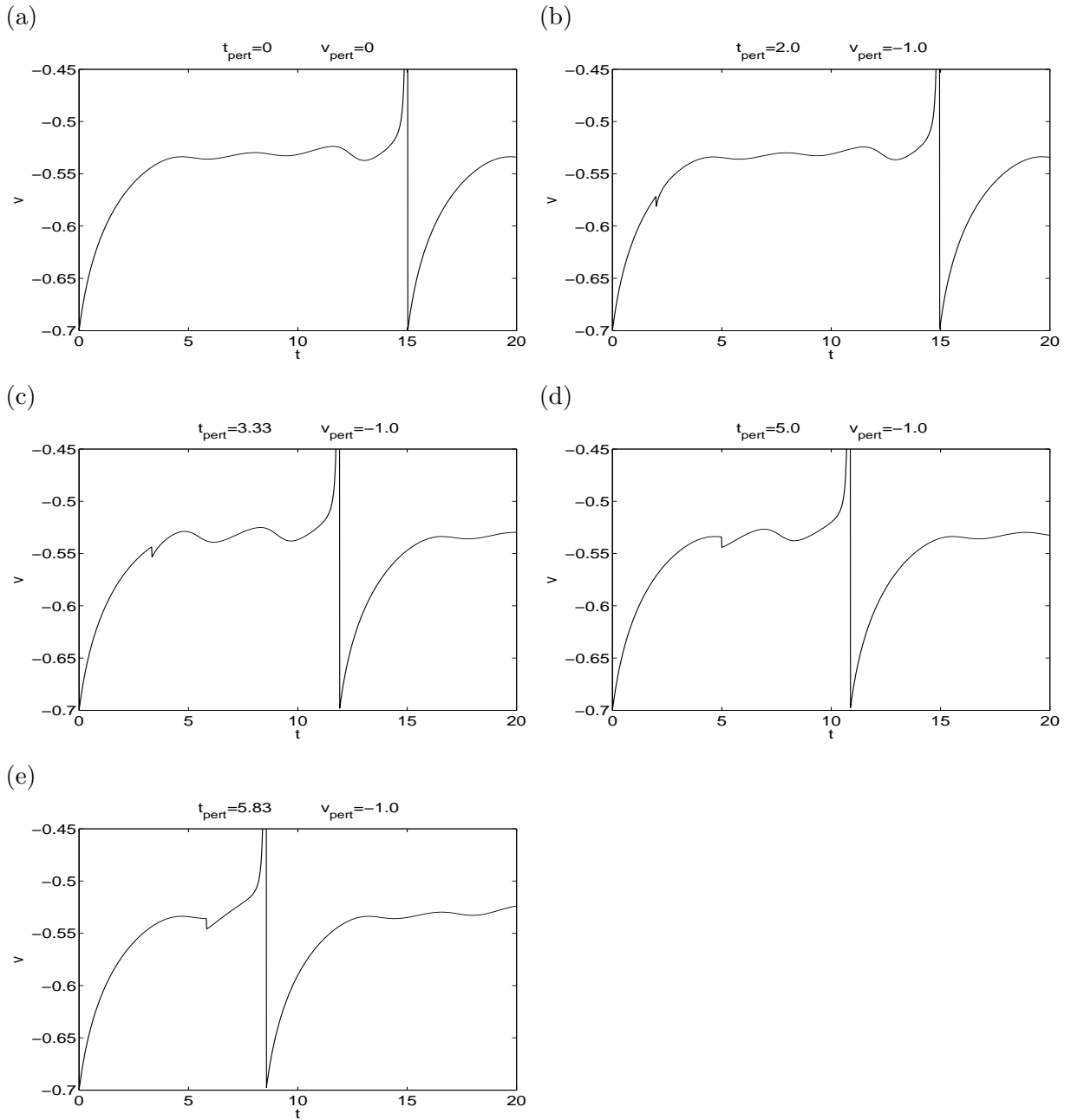


FIG. 15: Voltage traces showing the effect of inhibitory perturbations at various times  $t_{\text{pert}}$  on the mixed-mode oscillatory patterns corresponding to trajectories starting in a vicinity of the slow manifold for  $G_h = 1.5$  (1.0),  $I_{\text{app}} = -2.4$  ( $-0.0160$ ). The dimensionless values of  $G_h$  and  $I_{\text{app}}$  are given in parenthesis.